

1 TMEM135 is an LXR-Inducible Regulator of Peroxisomal Metabolism

2

3 Benjamin J. Renquist¹, Thushara W. Madanayake¹, Susma Ghimire¹, Caroline E. Geisler¹, Yafei

4 Xu¹, Randy L. Bogan*¹

5

6 ¹School of Animal & Comparative Biomedical Sciences, College of Agriculture & Life Sciences,

7 University of Arizona, Tucson, Arizona, 85721, USA

8

9 *Address correspondence to:

10 Randy L. Bogan, PhD, MCR

11 School of Animal and Comparative Biomedical Sciences

12 University of Arizona

13 PO Box 210090

14 Tucson, AZ 85721-0090

15 Phone: 520-621-1487

16 Fax: 520-621-9435

17 Email: boganr@email.arizona.edu

18

19

20

21 **Summary**

22 The liver x receptors (LXRs) are key regulators of systemic lipid metabolism. We identified
23 transmembrane protein 135 (TMEM135), a peroxisomal protein with an unknown function, as an
24 LXR target gene. The LXRs induce *TMEM135* transcription in humans via an LXR response
25 element located downstream of the putative transcriptional start site, but do not increase
26 *Tmem135* in murine cells. Functionally, knockdown of TMEM135 in hepatocytes *in vitro* and *in*
27 *vivo* results in fatty acid accumulation due to reduced peroxisomal β -oxidation, which was most
28 pronounced with elevated fatty acid loading. Mechanistically, proteomic and Western blot
29 analyses indicated that TMEM135 mediates import of peroxisome matrix proteins necessary for
30 β -oxidation and bile acid synthesis. These findings indicate that the LXRs regulate peroxisomal
31 metabolism via transcriptional control of *TMEM135*, and TMEM135 mediates an auxiliary matrix
32 protein import pathway and thus may serve as a therapeutic target for metabolic and aging
33 disorders associated with peroxisome dysfunction.

34 **Keywords:** peroxisome, liver x receptors, nuclear receptors, lipid metabolism, β -oxidation, liver
35 metabolism, steatosis, fatty acid metabolism, cholesterol, bile acid synthesis

36 **Introduction**

37 The liver x receptors (LXR) α (NR1H3) and β (NR1H2) belong to the nuclear receptor
38 superfamily and are key regulators of cholesterol and fatty acid metabolism (Hong and Tontonoz,
39 2014). Oxysterols are natural LXR ligands (Peet et al., 1998) that increase during cholesterol
40 loading. The LXRs heterodimerize with the retinoic acid receptor (RXR) and bind to LXR response
41 elements (LXRE) within the promoters of target genes (Peet et al., 1998). The LXREs belong to
42 the direct repeat 4 (DR4) class that consist of two hexanucleotide half-sites separated by a 4-
43 nucleotide spacer (Teboul et al., 1995; Willy et al., 1995). The protein products of known LXR
44 target genes affect systemic lipid metabolism. Well known examples include increasing
45 cholesterol efflux via ATP-binding cassette (ABC) sub-family A, member 1 (ABCA1) (Costet et
46 al., 2000), and sub-family G, member 1 (ABCG1) (Kennedy et al., 2001); limiting cholesterol

47 uptake via induction of myosin regulatory light chain interacting protein (MYLIP) that targets the
48 low-density lipoprotein receptor (LDLR) for ubiquitin-mediated degradation (Zelcer et al., 2009);
49 and increased lipogenesis via induction of sterol regulatory element binding protein 1c (SREBP1c,
50 encoded by sterol regulatory element binding transcription factor 1 gene or *SREBF1*) (Repa et
51 al., 2000; Yoshikawa et al., 2001). Also, the *NR1H3* isoform of the LXRs is itself an LXR target
52 gene (Laffitte et al., 2001; Whitney et al., 2001), leading to auto-amplification of LXR actions in
53 certain species and tissues. Although many LXR target genes have been discovered, additional
54 target genes may remain unidentified.

55 We have previously investigated LXR actions within the steroidogenic corpus luteum of
56 the ovary (Seto and Bogan, 2015; Xu et al., 2018a; Xu et al., 2018b). To uncover novel LXR target
57 genes, rhesus macaque luteal cells were treated with vehicle or 1 μ M T0901317 (T09, synthetic
58 LXR agonist) for 24 hours, mRNA were isolated and used for microarray analysis of gene
59 expression on the Affymetrix[®] Rhesus Macaque genome chip (unpublished data). Genes that
60 were differentially expressed (>2-fold change in T09 vs vehicle, $p < 0.05$ with Benjamini and
61 Hochberg correction for false discovery rate) were identified. Several known LXR target genes
62 were differentially expressed including *ABCA1*, *ABCG1*, *NR1H3*, *SREBF1*, and *MYLIP*. One gene
63 that was differentially expressed and not previously determined to be an LXR target gene was
64 transmembrane protein 135 (*TMEM135*). Therefore, the objective of the current study is to
65 determine if *TMEM135* is an LXR target gene and to identify its physiologic role in lipid
66 metabolism.

67 **Results**

68 LXR Agonist Increases Expression of TMEM135 in Human Hepatocyte and Macrophage Cell

69 Lines

70 Macrophage and hepatocyte cell lines were selected for initial studies on LXR regulation
71 of *TMEM135* transcription as these cell types play a pivotal role in LXR-mediated reverse
72 cholesterol transport from peripheral tissues to the liver (Hong and Tontonoz, 2014). The LXR

73 ligand T09 increased the mRNA expression of *TMEM135* in both HepG2 (Figure 1A) and Hep3B
74 (Figure 1B) hepatocyte cell lines, with an approximately 2-fold maximum increase in HepG2 cells
75 and a 3-fold increase in Hep3B cells. In monocyte-derived macrophages (THP-1), T09 also
76 induced *TMEM135* mRNA expression up to 4-fold (Figure 1C). The protein synthesis inhibitor
77 cycloheximide was used to determine whether the effect of T09 on *TMEM135* in THP-1 cells
78 requires synthesis of new proteins. Cycloheximide did not significantly affect basal or T09-
79 stimulated *TMEM135* mRNA expression (Figure 1D), indicating that T09 induces *TMEM135* via
80 a direct transcriptional mechanism not involving the synthesis of intermediary proteins. As
81 *TMEM135* has previously been reported to be localized to mitochondria (Exil et al., 2010; Lee et
82 al., 2016), the effect of T09 on *TMEM135* protein expression in mitochondria/peroxisome-
83 enriched fractions from HepG2 cells was determined. Relative concentrations of *TMEM135* were
84 significantly ($p < 0.05$) increased approximately 1.8-fold following a 24-hour T09 treatment (Figure
85 1E and 1F).

86 A LXRE Downstream of the Putative Transcription Start Site Mediates LXR Agonist Induction of 87 *TMEM135*

88 A 4 kb region spanning from -3319 to +682 bp (relative to the transcriptional start site) of
89 the human *TMEM135* promoter was analyzed with MatInspector (Cartharius et al., 2005) for
90 potential LXRE binding sites. This analysis yielded three potential LXREs (Figure S1), and these
91 were arbitrarily designated LXRE1, LXRE2 and LXRE3 in order from most distal to most proximal
92 to the translation start site. Electrophoretic mobility shift assays (EMSA) were used to determine
93 if LXR/RXR heterodimers bind these LXREs. As shown in Figure 2A, NR1H3 and RXRA nuclear
94 receptors together, but not individually, caused a shift in mobility of the fluorescent LXRE1 probe
95 indicating that NR1H3/RXRA heterodimers bind the LXRE1 sequence in the *TMEM135* promoter.
96 A 200-fold molar excess of unlabeled LXRE1, LXRE2, and LXRE3 oligonucleotides eliminated
97 the appearance of the shifted fluorescent band while the same molar excess of mutant LXRE1,
98 LXRE2, and LXRE3 oligonucleotides (Figure S1B) did not prevent NR1H3/RXRA binding to the

99 fluorescent probe; which validated the specificity of NR1H3/RXRA heterodimer binding to all 3
100 LXREs in the *TMEM135* promoter (Figure 2A). Similar results were obtained for NR1H2/RXRA
101 heterodimers (Figure 2B), indicating that both LXR isoforms specifically bind to all 3 LXRE sites
102 in the *TMEM135* promoter. The LXRE1 and LXRE2 sites have identical hexanucleotide half-sites,
103 whereas the LXRE3 site is unique (Figure S1B). To indicate if these sequence variations may
104 cause differences in relative binding affinity, a fluorescent LXRE3 probe was incubated with
105 NR1H3/RXRA heterodimers and increasing concentrations (from 0.25 to 10-fold molar excess) of
106 either LXRE1 or LXRE3 unlabeled competitor DNA. Oligonucleotides with the LXRE3 sequence
107 more effectively inhibited binding to the fluorescent probe than oligonucleotides with the LXRE1
108 sequence (Figure 2C). As a complementary approach, because the LXRE1 and LXRE3 sites
109 were fluorescently labelled with spectrally distinct fluorophores, an EMSA was performed where
110 a mixture of fluorescent LXRE1 and LXRE3 probes were incubated with increasing concentrations
111 of NR1H3/RXRA heterodimers. This approach resulted in a higher percentage of LXRE3 than
112 LXRE1 bound across a range of NR1H3/RXRA heterodimer concentrations (Figure 2D).
113 Collectively, this indicates that LXRE3 has a higher binding affinity for NR1H3/RXR heterodimers
114 than LXRE1.

115 Luciferase reporter assays were used to study transcription initiation from the *TMEM135*
116 promoter. Transfection of HepG2 cells with wild type *TMEM135* promoter/pGL 4.17 resulted in a
117 large increase in luciferase expression that was responsive to T09 as compared to the empty pGL
118 4.17 vector (Figure 2E). Furthermore, luciferase activity was further amplified by co-transfection
119 of plasmids that constitutively express NR1H3 and RXRA (Figure 2E). Next, we determined the
120 requirement of each individual LXRE to LXR agonist-induced transcription from the *TMEM135*
121 promoter. Promoters containing all combinations of wild type and mutant LXREs (Figure S1B)
122 were generated, and T09-induced luciferase activity was determined. LXR-agonist induced
123 luciferase activity was significantly ($p < 0.05$) higher in cells transfected with the wild type
124 *TMEM135* promoter as compared to the *TMEM135* promoter with all 3 LXREs mutated (Figure

125 2F). Furthermore, constructs containing the wild type LXRE3 site and mutated LXRE1 and/or
126 LXRE2 sites were not significantly different from the wild type promoter, while all constructs that
127 contained a mutated LXRE3 were not significantly different from the promoter that had all three
128 LXREs mutated (Figure 2F). This indicates that even though all 3 LXREs bind LXR/RXR
129 heterodimers, the LXRE3 site alone mediates LXR agonist-induced transcription from the
130 *TMEM135* promoter.

131 We next determined whether *Tmem135* mRNA expression was induced by T09 in mice.
132 The murine LXRE3 site showed relatively little homology with the human sequence as a total of
133 3 nucleotides within both hexanucleotide half-sites were unique in mice (Figure S2A). In mouse
134 hepatocyte (BNL 1NG A.2) and macrophage (RAW 264.7) cell lines, T09 did not significantly
135 induce *Tmem135* mRNA expression (Figure S2B) whereas it did increase the known LXR target
136 gene *Abca1* (Figure S2C). These data indicate that *Tmem135* is not an LXR target gene in mice.

137 *TMEM135* is a Direct Target Gene of the LXRs

138 To directly determine whether the LXRs are needed for T09-induced *TMEM135*
139 transcription, siRNA-mediated knockdown of the LXRs was performed in HepG2 cells. The
140 *NR1H2* siRNA caused an approximately 75% decrease ($p < 0.05$) in *NR1H2* mRNA expression
141 compared to the control and *NR1H3* siRNA groups (Figure 3A). The *NR1H3* siRNA resulted in an
142 approximately 70-80% decrease ($p < 0.05$) in *NR1H3* mRNA expression compared to the control
143 siRNA depending on the presence or absence of T09 (Figure 3B). The *NR1H2* siRNA by itself
144 also caused a significant reduction in T09-stimulated *NR1H3* mRNA expression and tended to
145 slightly improve *NR1H3* knockdown when co-transfected with the *NR1H3* siRNA (Figure 3B).
146 Decreased *NR1H3* mRNA expression is expected to occur following *NR1H2* knockdown because
147 *NR1H3* itself is an LXR target gene (Kennedy et al., 2001; Whitney et al., 2001). Consistent with
148 *NR1H3* being an LXR target gene, T09 induced a significant increase in *NR1H3* in the control
149 siRNA group, while T09 was not as effective at inducing *NR1H3* in the *NR1H2* siRNA group
150 (Figure 3B).

151 The known LXR target gene *ABCA1* was significantly increased by T09 in the control
152 siRNA group, and the effect of T09 was completely abolished by *NR1H2/NR1H3* siRNA co-
153 transfection (Figure 3C). Also, *NR1H3* knockdown alone significantly inhibited the T09-induced
154 increase in *ABCA1* (Figure 3C). Results for *TMEM135* were very similar to *ABCA1* with T09
155 causing a significant increase in the control siRNA group, and the effect of T09 was completely
156 blocked by *NR1H2/NR1H3* siRNA co-transfection (Figure 3D). Furthermore, *NR1H3* knockdown
157 itself significantly inhibited the T09-induced increase in *TMEM135* as compared to the control
158 siRNA (Figure 3D).

159 The LXRE3 site of the human *TMEM135* promoter lies downstream of the putative
160 transcriptional start site, but before the translation initiation site (Figure S1). To determine whether
161 LXR-mediated transcription of *TMEM135* results in an mRNA with a truncated 5' UTR, primers
162 and a probe were designed to amplify and detect a 76 base pair region encompassing the LXRE3
163 site in the 5' UTR. There was a significant ($p < 0.05$) reduction in mRNA expression of full-length
164 5' UTR transcripts caused by T09 in the control siRNA group, while this effect was blocked by
165 *NR1H2/NR1H3* siRNA co-transfection (Figure 3E). Furthermore, *NR1H2/NR1H3* co-knockdown
166 resulted in a significant ($p < 0.05$) increase in basal mRNA expression of full-length 5' UTR
167 transcripts compared to all other groups (Figure 3E). ChIP was used to determine if the reduction
168 in full-length 5' UTR transcripts is associated with increased NR1H2 and/or NR1H3 binding to the
169 LXRE3 site on the *TMEM135* gene. Monoclonal antibodies specific for each LXR isoform were
170 used for ChIP, and QPCR of the LXRE3 region on chromatin purified via ChIP indicated that T09
171 treatment caused a significant increase in binding of NR1H3 to LXRE3 in the *TMEM135* gene
172 (Figure 3F). This indicates that LXR binding to LXRE3 increases mRNA expression of *TMEM135*
173 via a transcript with a truncated 5' UTR relative to the putative mRNA sequence.

174 TMEM135 Mediates Fatty Acid Metabolism and Proliferation in HepG2 Cells

175 To begin unraveling the biologic function of *TMEM135*, a series of knockdown experiments
176 were performed. Transfection of HepG2 cells with siRNA against *TMEM135* decreased its mRNA

177 expression by 70-90%. As TMEM135 has previously been implicated in fat metabolism (Exil et
178 al., 2010), and the LXRs are known to induce lipogenesis (Hong and Tontonoz, 2014), we first
179 determined its effect on triglycerides and mRNA expression of fatty acid oxidation and
180 lipogenesis-associated genes. Knockdown of TMEM135 significantly increased basal triglyceride
181 accumulation in HepG2 cells (Figure 4A). Furthermore, T09 significantly increased intracellular
182 triglyceride concentrations, while TMEM135 knockdown further increased triglyceride
183 accumulation in the presence of T09 (Figure 4A). An increase in triglyceride accumulation could
184 result from a decrease in fatty acid oxidation and/or an increase in lipogenesis. There were no
185 significant effects of TMEM135 knockdown on mRNA expression of the key regulator of fatty acid
186 β -oxidation, peroxisome proliferator activated receptor alpha (*PPARA*), while it tended to increase
187 the *PPARA* target gene carnitine palmitoyltransferase 1A (*CPT1A*) (Kersten and Stienstra, 2017)
188 (Figure 4B). It is known that the LXRs induce lipogenesis via induction of SREBP1c (*SREBF1*
189 gene) (Repa et al., 2000; Yoshikawa et al., 2001). As expected, T09 caused a significant increase
190 in *SREBF1* and the SREBP1c/LXR target gene fatty acid synthase (*FASN*) (Figure 4B), consistent
191 with the T09-induced increase in triglyceride accumulation (Figure 4A). However, TMEM135
192 knockdown significantly suppressed both basal and T09-induced *SREBF1* mRNA expression
193 (Figure 4B). This indicates that the increase in triglyceride accumulation in HepG2 cells occurred
194 despite an apparent reduction in lipogenesis. Thus, an inhibition of fatty acid oxidation seems a
195 more likely explanation for the increase in triglycerides. The tendency for an increase in *CPT1A*
196 mRNA caused by TMEM135 knockdown is not evidence against a decrease in fatty acid oxidation
197 because reduced β -oxidation would result in fatty acid accumulation, and because fatty acids are
198 the endogenous ligands for *PPARA* (Kersten and Stienstra, 2017), this would also cause
199 increased *CPT1A* mRNA expression. Further supporting an impairment in fatty acid β -oxidation,
200 TMEM135 knockdown significantly reduced ATP concentrations when HepG2 cells were
201 incubated in glucose-free medium (Figure 4C).

202 During these experiments it appeared that TMEM135 knockdown also inhibited replication
203 of HepG2 cells. Because enhanced β -oxidation is a hallmark of hepatocellular carcinoma (HCC)
204 (Beyoglu and Idle, 2013) and our previous experiments indicated a key role for TMEM135 in fatty
205 acid metabolism, we determined whether TMEM135 regulated proliferation of HepG2 cells.
206 Knockdown of *TMEM135* significantly ($p < 0.05$) reduced viable HepG2 cell numbers at 48 and 72
207 hours post-transfection as compared to cells transfected with the control siRNA (Figure 4D). Cell
208 cycle analysis indicated that *TMEM135* knockdown significantly ($p < 0.05$) increased the
209 percentage of HepG2 cells in the G0/G1 stage, with a corresponding significant reduction in the
210 percentage of cells in the S phase (Figure 4E). The increase in G0/G1 arrest was associated with
211 alterations in mRNA expression of tumor suppressor and cell cycle genes. There were significant
212 increases in cyclin dependent kinase inhibitor 2A (*CDKN2A*) and tumor protein p53 (*TP53*) (Figure
213 4F), which restrict passage through the G1/S checkpoint (LaPak and Burd, 2014). There were
214 also significant increases in cyclin dependent kinase 2 (*CDK2*) and cyclin E1 (*CCNE1*) (Figure
215 4F), which increase prior to passage through the G1/S checkpoint, but no change in cyclin A2
216 (*CCNA2*) (Figure 4F) which is increased in the S phase (Harper and Adams, 2001). Collectively,
217 these data indicate that TMEM135 knockdown reduces HepG2 proliferation by restricting passage
218 through the G1/S checkpoint.

219 Liver-Selective TMEM135 Knockdown Reduces Peroxisomal β -Oxidation

220 To determine the physiologic function of TMEM135, a siRNA knockdown experiment was
221 performed in male C57BL/6 mice. Mice received either a non-targeting control or *Tmem135*
222 siRNA and were sacrificed 4 days later in either the *ad libitum* fed state or after a 12-hour fast.
223 Because we determined that *Tmem135* is not an LXR target gene in mice (Figure S2), we used
224 fasting to induce hepatic fat accumulation. The *Tmem135* siRNA caused an approximately 60%
225 mRNA knockdown in the liver while no knockdown was observed in other tissues including
226 skeletal muscle, adipose, and heart (Figure 5A). Knockdown of TMEM135 in the liver was further
227 confirmed by Western blot and proteomic analysis of mitochondria/peroxisome-enriched fractions

228 (Figure 5B). Fed mice injected with the *Tmem135* siRNA gained significantly less weight during
229 the 4-day treatment, while the loss in weight from fasting was similar for both siRNAs (Figure 5C).
230 There was no significant effect of the *Tmem135* siRNA on basal or fasting-induced hepatic
231 triglycerides (Figure S3A), while there was a tendency for increased hepatic non-esterified fatty
232 acid (NEFA) concentrations in TMEM135 knockdown mice in the fed state (Figure S3B). There
233 were no significant effects of TMEM135 knockdown on liver ATP or glycogen concentrations
234 (Figure S3C-D). Also, there were no significant effects of TMEM135 on serum lipids (total
235 cholesterol, HDL cholesterol, triglycerides), although there was a trend for fasting to reduce serum
236 triglycerides in control siRNA mice that was not observed in TMEM135 knockdown mice (Figure
237 S4A). There were no significant effects of TMEM135 knockdown on serum NEFA, glucose,
238 insulin, or β -hydroxybutyrate concentrations (Figure S4B-E). The mRNA expression of key genes
239 involved in fatty acid β -oxidation were determined in the liver. As expected, fasting significantly
240 induced mRNA expression of *Ppara*, *Cpt1a*, acyl-CoA dehydrogenase medium chain (*Acadm*),
241 uncoupling protein 2 (*Ucp2*), and sirtuin 3 (*Sirt3*) (Figure 5D). Similarly, knockdown of TMEM135
242 significantly increased *Acadm* and *Sirt3* in fed animals, while *Ucp2* was significantly reduced by
243 TMEM135 knockdown in fasted animals (Figure 5D). As expected with increased β -oxidative flux,
244 fasting significantly increased NADH in animals receiving the control siRNA, while TMEM135
245 knockdown significantly reduced NADH (Figure 5E) indicating an impairment in β -oxidation in
246 fasted mice. Reduced hepatic NADH during fasting could be due to reduced β -oxidation in
247 peroxisomes and/or mitochondria. However, there was a reciprocal significant increase in hepatic
248 ketone concentrations in fasted mice with TMEM135 knockdown (Figure 5F). Because
249 ketogenesis occurs exclusively in mitochondria and is intricately linked with fatty acid oxidation
250 (Newman and Verdin, 2017), this indicates that mitochondrial fatty acid β -oxidation was not
251 impaired. Thus, knockdown mice have impaired fatty acid β -oxidation in peroxisomes but not
252 mitochondria.

253 TMEM135 Knockdown Reduces Import of Peroxisome Matrix Enzymes

254 TMEM135 is a peroxisomal protein with high homology to the Tim17 family that mediate
255 translocation of proteins across mitochondrial membranes (Zarsky and Dolezal, 2016). In addition
256 to peroxisomes, TMEM135 has been reported to be localized to mitochondria (Exil et al., 2010;
257 Lee et al., 2016). Therefore, we hypothesized that TMEM135 mediates protein import into
258 peroxisomes and/or mitochondria. A mitochondria/peroxisome-enriched fraction was prepared
259 from frozen mouse livers. This fraction was validated to contain both mitochondria and
260 peroxisomes as indicated by presence of the mitochondria marker cytochrome c oxidase subunit
261 4I1 (COX4I1) and the peroxisome marker ATP binding cassette subfamily D member 3 (ABCD3,
262 also known as PMP70), while COX4I1 and ABCD3 were not detected in the cytosolic fraction
263 (Figure 6A). Furthermore, the cytosolic protein tubulin beta class I (TUBB) segregated to the
264 cytosolic fraction and was not detected in the mitochondria/peroxisome-enriched fraction.
265 Proteomic analysis of a subset of fed mice was used to provide an unbiased estimate of
266 differential protein abundance in the mitochondria/peroxisome-enriched fractions. A total of 23
267 proteins were significantly less abundant (Fisher's Exact Test, $p < 0.05$) in the
268 mitochondria/peroxisome-enriched fraction from TMEM135 knockdown livers (Figure 6B).
269 Interestingly, these 23 proteins included nearly all the matrix proteins known to be necessary for
270 peroxisomal bile acid synthesis and β -oxidation of very-long chain fatty acids, branched chain
271 fatty acids, and dicarboxylic acids (Baes and Van Veldhoven, 2016; Waterham et al., 2016)
272 (Figure 6 C-D). Analysis of ABCD3 expression by proteomic and Western blot analysis
273 demonstrated that total peroxisome content was not significantly altered by TMEM135 knockdown
274 (Figure 6E), indicating that the lower abundance of peroxisomal proteins in the proteomic data
275 was not simply due to reduced peroxisome content. Four peroxisomal proteins were selected for
276 further analysis via Western blot: acetyl-CoA acyltransferase 1 (ACAA1), acyl-CoA oxidase 1
277 (ACOX1), sterol carrier protein 2 (SCP2), and catalase (CAT). All these proteins were enriched in
278 the mitochondria/peroxisome fraction, but except for SCP2 (which had low detection sensitivity)
279 each protein was also clearly detectable in the cytosolic fraction (Figure 6F). This contrasts with

280 the peroxisome membrane protein ABCD3 which appeared to be exclusively localized to the
281 mitochondria/peroxisome fraction (Figure 6A). Collectively, detection of these proteins in the
282 cytoplasm indicates that their import into peroxisomes may be rate-limiting.

283 We next used Western blot to quantitatively determine import of ACAA1, ACOX1, SCP2,
284 and CAT into peroxisomes. Whole cell lysates (using TUBB as loading control) and
285 mitochondria/peroxisome-enriched fractions (using ABCD3 as loading control for peroxisomes)
286 were analyzed (Figure 7A). The signal for each protein was normalized to the respective loading
287 control, and the ratio of peroxisome to whole cell lysate was used to determine import. Using this
288 method, there were no significant differences between siRNAs for peroxisome import of ACOX1
289 and CAT in either fed or fasted animals (Figure 7B). However, relative ACAA1 import was
290 significantly reduced in TMEM135 knockdown mice when fasted (Figure 7B). Furthermore, SCP2
291 import was significantly lower in TMEM135 knockdown mice in both the fed and fasted state
292 (Figure 7B). Collectively, Western blot confirmed that TMEM135 mediates the import of ACAA1
293 and SCP2 into peroxisomes, and thus may mediate the import of additional proteins identified via
294 proteomics.

295 TMEM135 Knockdown Inhibits Fasting-Induced β -Oxidation

296 We next determined the effect of TMEM135 on markers of peroxisome function. In fasted
297 mice, TMEM135 knockdown resulted in a significant increase in total fatty acids and linoleic acid,
298 with trends ($0.05 < p < 0.1$) for increases in several other fatty acids (Figure 7C-D). In general,
299 mitochondria preferentially oxidize short and medium chain fatty acids (<C12), both mitochondria
300 and peroxisomes oxidize long chain fatty acids (C14-C18), while peroxisomes exclusively oxidize
301 very-long chain fatty acids (>C20) (Cipolla and Lodhi, 2017). While mitochondria are believed to
302 be the principal site of long chain fatty acid oxidation, peroxisomes also directly oxidize long chain
303 fatty acids in a cooperative manner with mitochondria (Noland et al., 2007). The peroxisomal
304 contribution to long chain fatty acid oxidation becomes quantitatively greater during physiologic
305 states of increased fatty acid load such as fasting, diabetes, and high fat diets (Baes and Van

306 Veldhoven, 2016). The significant increase in linoleic and total fatty acids is consistent with an
307 impairment in β -oxidation in fasted TMEM135 knockdown mice, and when considering hepatic
308 NADH and ketone concentrations (Figure 5E-F), indicates that the impairment occurred in
309 peroxisomes. Also, linoleic acid is an essential fatty acid obtained via dietary sources (Saini and
310 Keum, 2018), which indicates that TMEM135 is not altering fatty acid synthesis or desaturation.
311 With the exception of 22:6 that is derived from 18:3 (Saini and Keum, 2018), fasting itself did not
312 increase any of the very-long chain fatty acids that are exclusively oxidized by peroxisomes and
313 may explain why TMEM135 knockdown did not affect very-long chain fatty acid concentrations in
314 fasted mice. Interestingly, in fed mice TMEM135 knockdown significantly decreased 22:0 and
315 tended to decrease 24:0, indicating a slight increase in peroxisomal β -oxidation in the fed state.
316 Regarding bile acids, hepatic concentrations of cholic acid were not significantly altered by
317 TMEM135 knockdown (Figure S5). Collectively, these data indicate that TMEM135 may not be
318 obligatory to basal peroxisome function, but under physiologic conditions of elevated hepatic fatty
319 acid flux, TMEM135 may play a key role in enhancing peroxisomal function to assist the liver in
320 meeting the increased demand for β -oxidation.

321 **Discussion**

322 Peroxisomes have key catabolic functions including α and β -oxidation of fatty acids, and
323 anabolic activities including the synthesis of bile acids and ether phospholipids (Baes and Van
324 Veldhoven, 2016; Waterham et al., 2016). There are 2 main classes of peroxisome disorders: 1)
325 peroxisome biogenesis disorders, and 2) single peroxisomal enzyme deficiencies (Baes and Van
326 Veldhoven, 2016; Waterham et al., 2016). Outcomes from these disorders range from infant death
327 to mild degenerative neurosensory problems (Baes and Van Veldhoven, 2016; Waterham et al.,
328 2016). Hepatic pathologies are one of the principal features associated with peroxisome
329 disorders, which are often caused by a failure to import matrix enzymes into peroxisomes (Baes
330 and Van Veldhoven, 2016). In the current study we determined that TMEM135 is an LXR-

331 inducible protein that regulates peroxisome function by mediating an auxiliary import pathway for
332 matrix enzymes to enter peroxisomes.

333 Multiple lines of evidence support TMEM135 as being a regulator of peroxisome function.
334 When hepatic β -oxidation (both peroxisomal and mitochondrial) was stimulated by fasting,
335 TMEM135 knockdown mice had significantly lower NADH (Figure 5E) and significantly higher
336 total fatty acid and linoleic acid concentrations (Figure 7C-D), indicating an impairment in β -
337 oxidation. Meanwhile, hepatic ketones were significantly increased in knockdown mice when
338 fasted (Figure 5F), and ketogenesis occurs exclusively in mitochondria and is intricately linked to
339 β -oxidation (Newman and Verdin, 2017). Collectively, these findings indicate that β -oxidation was
340 impaired in peroxisomes, but not in mitochondria. The increase in ketones may have resulted
341 from the increased availability of fatty acids to the mitochondria and/or due to the increased
342 NAD⁺/NADH ratio, both of which stimulate ketogenesis (Newman and Verdin, 2017). Additionally,
343 many effects of hepatocyte-specific TMEM135 knockdown in the current study are consistent with
344 typical features of peroxisome dysfunction. Liver-specific peroxisome deficiency in mice
345 (peroxisomal biogenesis factor 5 or *Pex5* conditional knockout) results in hepatic fat accumulation
346 despite significantly reduced mRNA expression of *Srebf1* and increased PPARA target gene
347 mRNA expression, and a stunting of body growth (Peeters et al., 2011). In our study, knockdown
348 of TMEM135 caused fatty acid accumulation both *in vitro* and *in vivo*. In HepG2 cells, increased
349 triglycerides occurred despite a simultaneous significant reduction in mRNA expression of
350 *SREBF1* (Figure 4A-B), and some PPARA target genes were increased by TMEM135 knockdown
351 in fed mice (Figure 5D). Also, TMEM135 knockdown caused a significant reduction in body weight
352 gain of knockdown mice in the fed state (Figure 5C). Collectively, these data indicate that
353 TMEM135 mediates peroxisome function.

354 Mechanistically, our data indicate that TMEM135 modulates peroxisome function by
355 regulating the import of matrix enzymes into peroxisomes. This differs from the classical
356 mechanism involving peroxisomal targeting signals (PTS), which are short amino acid sequences

357 at the N or C-terminus that interact with various members of the peroxin family of proteins to
358 facilitate import into the peroxisome matrix (Haimovich et al., 2016). Among the proteins whose
359 import was quantified by Western blot in the current study ACOX1 and SCP2 contain a PTS1
360 sequence on their C-terminus that is recognized by PEX5, and ACAA1 contains a PTS2 sequence
361 at its N-terminus that interacts with PEX7 (peroxisomal biogenesis factor 7) (Haimovich et al.,
362 2016; Mizuno et al., 2013). Therefore, TMEM135 is likely not obligatory for their import, but rather
363 serves an auxiliary role. It is not known whether TMEM135-mediated protein import occurs via a
364 mechanism that involves, or occurs independently of, peroxins. Because TMEM135 is a
365 transmembrane protein with TIM17 homology (Zarsky and Dolezal, 2016), a peroxin-independent
366 mechanism seems most likely. Regardless, TMEM135-mediated protein import may be
367 necessary under conditions of high peroxisome activity when peroxin-dependent import becomes
368 saturated, which is consistent with our finding that fasting-induced hepatic β -oxidation is
369 dependent on TMEM135.

370 An auxiliary role of TMEM135 in peroxisome protein import makes it a potential therapeutic
371 target, and because it is also an LXR target gene in humans, pharmacologic modulation of the
372 LXRs may be useful for altering peroxisome metabolism. The LXRs are master regulators of
373 reverse cholesterol transport (RCT), a process whereby excess cholesterol is removed from
374 peripheral tissues and transported to the liver for elimination in bile acids (Hong and Tontonoz,
375 2014). There has been much interest in the development of LXR agonists to treat human diseases
376 including atherosclerosis, Alzheimer's disease, and other metabolic disorders (Hong and
377 Tontonoz, 2014). However, the therapeutic potential of LXR agonists has been limited because
378 they also increase hepatic lipogenesis via induction of SREBP1c (Repa et al., 2000; Yoshikawa
379 et al., 2001). Our data indicate that the LXRs can stimulate peroxisomal β -oxidation by increasing
380 transcription of *TMEM135*, which consequently may limit steatosis during LXR-induced
381 lipogenesis. It should be noted that our data indicate that *TMEM135* is an LXR target gene in
382 humans, but in mice *Tmem135* is either not induced by the LXRs or is a low-affinity target gene

383 (Figure S2). Thus, LXR agonist-induced steatosis may be less pronounced in human compared
384 to mice hepatocytes due to species differences in LXR regulation of *TMEM135* transcription.
385 Previous evidence of a link between the LXRs and peroxisomal β -oxidation is limited and
386 conflicting. One group reported increased hepatic peroxisomal β -oxidation in mice treated with an
387 LXR agonist through an undefined mechanism involving increased oxidative gene expression
388 (Beyer et al., 2004; Hu et al., 2005). However, another report indicates that the LXRs suppress
389 peroxisomal β -oxidation by inhibiting expression of the peroxisomal membrane transporter
390 ABCD2 (Gondcaille et al., 2014). It would be interesting to determine how LXR-mediated
391 suppression of ABCD2 and induction of *TMEM135* influences overall peroxisome function.

392 Elevated *TMEM135* may protect against lipid loading but may also contribute to hepatic
393 pathologies. For example, metabolomics studies have reported that elevated serum bile acids
394 and urinary bile salts represent the core metabolic phenotype in the transition from healthy liver
395 to nonalcoholic fatty liver disease, nonalcoholic steatohepatitis, cirrhosis, and HCC (Beyoglu and
396 Idle, 2013). Additionally, elevated β -oxidation and reduced mitochondrial respiration are part of
397 the metabolic remodeling that occurs in chronic liver disease (Beyoglu and Idle, 2013). These
398 metabolic changes are consistent with high peroxisome activity as peroxisomes play a key role in
399 bile acid synthesis, they contribute to fatty acid β -oxidation, and can also indirectly alter
400 mitochondrial respiration (Baes and Van Veldhoven, 2016). In the current study *TMEM135*
401 knockdown reduced proliferation of the HepG2 cell line by increasing G0/G1 arrest. Also, a
402 metabolomics study found that linoleic acid is significantly reduced in human HCC tumors
403 compared to nontumor liver tissue from the same subjects (Beyoglu et al., 2013), and in our data
404 linoleic acid was significantly increased by *TMEM135* knockdown *in vivo* (Figure 7C), consistent
405 with a role for *TMEM135* in pathogenic β -oxidation. There is additional evidence in the literature
406 of an oncogenic role for *TMEM135*. It was among genes identified by transcriptomic analysis as
407 being significantly reduced in expression when proliferation of HepG2 and Huh7 cells were
408 inhibited by knockdown of the COP9 signalosome subunit 5 (Lee et al., 2011). Also, a genomic

409 rearrangement that results in a TMEM135-containing fusion transcript has been linked with
410 aggressive prostate cancer (Yu et al., 2014), and Cas9-mediated insertion of a suicide gene into
411 cells expressing this same fusion transcript reduces tumor burden and mortality in mouse
412 xenografts (Chen et al., 2017). Thus, TMEM135 may represent a novel target in the treatment of
413 certain cancers and chronic liver disease.

414 Previous studies to determine the biological function of TMEM135 are limited. The first
415 indication of its function came from a mouse model of mitochondrial acyl-CoA dehydrogenase
416 very long chain (ACADVL) deficiency (Exil et al., 2010). Under conditions of increased demand
417 for β -oxidation such as fasting and cold stress, ACADVL-deficient mice have reduced survival
418 due to cardiac dysfunction (Exil et al., 2010). It was discovered that TMEM135 was elevated more
419 than four-fold in the hearts of ACADVL-deficient mice that survived birth (Exil et al., 2010). The
420 ACADVL enzyme catalyzes the first step in mitochondrial β -oxidation using fatty acids larger than
421 14 carbons as substrates (McAndrew et al., 2008). Because ACADVL deficiency restricts the
422 mitochondria from directly oxidizing long chain fatty acids, data from the current study indicate
423 that the increase in TMEM135 likely promoted survival by increasing peroxisomal β -oxidation and
424 the processing of long and very-long chain fatty acids to medium chain fatty acids that were
425 subsequently oxidized in the mitochondria in an ACADVL-independent manner. Another study
426 into TMEM135 function reported that a mutation in *Tmem135* was responsible for accelerated
427 aging of the retina in a mouse model of age-related macular degeneration (Lee et al., 2016).
428 Neurodegenerative disorders are commonly associated with peroxisome dysfunction (Cipolla and
429 Lodhi, 2017), which is consistent with a *Tmem135* mutation causing accelerated aging in the
430 retina. Both of these previous studies on TMEM135 reported that it is localized to mitochondria
431 (Exil et al., 2010; Lee et al., 2016), whereas our data indicates it functions in peroxisomes. In
432 support of a peroxisomal origin of action, another previous study clearly demonstrated that
433 TMEM135 (formerly known as PMP52) is localized to peroxisomes and not mitochondria (Wiese
434 et al., 2007). Because peroxisomes and mitochondria can physically associate via the formation

435 of tethering complexes (Schrader et al., 2015), it seems likely that reports of TMEM135
436 association with mitochondria (Exil et al., 2010; Lee et al., 2016) were due to peroxisomes that
437 were tethered to mitochondria, and TMEM135 effects on mitochondria are indirectly mediated via
438 altered peroxisome function.

439 The critical role of peroxisomes in human health is illustrated by the spectrum of
440 peroxisome disorders; but in addition to these inborn errors of metabolism it is becoming
441 increasingly apparent that peroxisomes play key roles in other metabolic and age-related
442 diseases including cancer, neurodegenerative disorders, and diabetes (Cipolla and Lodhi, 2017).
443 This may be due to direct catabolic and anabolic actions of peroxisomes, as well as interactions
444 between peroxisomes and other organelles including mitochondria (Cipolla and Lodhi, 2017;
445 Schrader et al., 2015). Our data indicate that TMEM135 regulates peroxisome function by
446 mediating an auxiliary matrix protein import pathway. Furthermore, the effects of TMEM135 are
447 inducible as it is an LXR target gene in humans, and it is likely to be regulated by other metabolic
448 signaling pathways. In support of this, PPARA is the master regulator of β -oxidation in the liver
449 and in primary human hepatocytes *TMEM135* mRNA expression is consistently induced by
450 PPARA agonists (Kersten and Stienstra, 2017) and its promoter is bound by PPARA as
451 determined using ChIP-seq (McMullen et al., 2014), indicating it is also a PPARA target gene.
452 These findings implicate TMEM135 as a potential therapeutic target in the treatment of metabolic
453 and age-related diseases that are associated with peroxisome dysfunction.

454 **Acknowledgements**

455 Mass spectrometry and proteomics data were acquired by the Arizona Proteomics
456 Consortium at the BIO5 Institute of the University of Arizona. The authors would like to thank Dr.
457 Jon Hennebold at the Oregon National Primate Research Center of Oregon Health & Science
458 University for assistance with the unpublished microarray experiment in macaque luteal cells that
459 provided preliminary data for the current study. The authors would also like to thank Dr. André-
460 Denis Wright for arranging Departmental support to ensure completion of this project. This

461 research was supported by the Eunice Kennedy Shriver National Institute of Child Health &
462 Human Development, National Institutes of Health, Award Number R00 HD067678 to R.L.B. The
463 content is solely the responsibility of the authors and does not necessarily represent the official
464 views of the National Institutes of Health. This work was also supported by the Arizona Biomedical
465 Research Commission Early Stage Investigator Award No. ADHS14-082986 to B.J.R.

466 **Author Contributions**

467 Conceptualization, R.L.B. and B.J.R.; Methodology R.L.B. and B.J.R.; Investigation,
468 R.L.B., B.J.R., T.W.M., S.G., C.E.G., and Y.X.; Resources, R.L.B. and B.J.R.; Writing – Original
469 Draft, R.L.B.; Writing – Review & Editing, R.L.B. and B.J.R.; Funding Acquisition, R.L.B. and
470 B.J.R.

471 **Declaration of Interests**

472 The authors declare no competing interests.

473 **References**

- 474 Baes, M., and Van Veldhoven, P.P. (2016). Hepatic dysfunction in peroxisomal disorders. *Biochim*
475 *Biophys Acta* 1863, 956-970.
- 476 Beyer, T.P., Schmidt, R.J., Foxworthy, P., Zhang, Y., Dai, J., Bensch, W.R., Kauffman, R.F., Gao,
477 H., Ryan, T.P., Jiang, X.C., et al. (2004). Coadministration of a liver X receptor agonist
478 and a peroxisome proliferator activator receptor- α agonist in Mice: effects of nuclear
479 receptor interplay on high-density lipoprotein and triglyceride metabolism in vivo. *J*
480 *Pharmacol Exp Ther* 309, 861-868.
- 481 Beyoglu, D., and Idle, J.R. (2013). The metabolomic window into hepatobiliary disease. *J Hepatol*
482 59, 842-858.
- 483 Beyoglu, D., Imbeaud, S., Maurhofer, O., Bioulac-Sage, P., Zucman-Rossi, J., Dufour, J.F., and
484 Idle, J.R. (2013). Tissue metabolomics of hepatocellular carcinoma: tumor energy
485 metabolism and the role of transcriptomic classification. *Hepatology* 58, 229-238.
- 486 Cartharius, K., Frech, K., Grote, K., Klocke, B., Haltmeier, M., Klingenhoff, A., Frisch, M.,
487 Bayerlein, M., and Werner, T. (2005). MatInspector and beyond: promoter analysis based
488 on transcription factor binding sites. *Bioinformatics* 21, 2933-2942.
- 489 Chen, Z.H., Yu, Y.P., Zuo, Z.H., Nelson, J.B., Michalopoulos, G.K., Monga, S., Liu, S., Tseng, G.,
490 and Luo, J.H. (2017). Targeting genomic rearrangements in tumor cells through Cas9-
491 mediated insertion of a suicide gene. *Nat Biotechnol* 35, 543-550.
- 492 Cipolla, C.M., and Lodhi, I.J. (2017). Peroxisomal Dysfunction in Age-Related Diseases. *Trends*
493 *Endocrinol Metab* 28, 297-308.
- 494 Costet, P., Luo, Y., Wang, N., and Tall, A.R. (2000). Sterol-dependent transactivation of the ABC1
495 promoter by the liver X receptor/retinoid X receptor. *J Biol Chem* 275, 28240-28245.
- 496 Exil, V.J., Silva Avila, D., Benedetto, A., Exil, E.A., Adams, M.R., Au, C., and Aschner, M. (2010).
497 Stressed-induced TMEM135 protein is part of a conserved genetic network involved in fat
498 storage and longevity regulation in *Caenorhabditis elegans*. *PLoS One* 5, e14228.

- 499 Geisler, C.E., Hepler, C., Higgins, M.R., and Renquist, B.J. (2016). Hepatic adaptations to
500 maintain metabolic homeostasis in response to fasting and refeeding in mice. *Nutr Metab*
501 (Lond) *13*, 62.
- 502 Gondcaille, C., Genin, E.C., Lopez, T.E., Dias, A.M., Geillon, F., Andreoletti, P., Cherkaoui-Malki,
503 M., Nury, T., Lizard, G., Weinhofer, I., et al. (2014). LXR antagonists induce ABCD2
504 expression. *Biochim Biophys Acta* *1841*, 259-266.
- 505 Haimovich, G., Cohen-Zontag, O., and Gerst, J.E. (2016). A role for mRNA trafficking and
506 localized translation in peroxisome biogenesis and function? *Biochim Biophys Acta* *1863*,
507 911-921.
- 508 Harper, J.W., and Adams, P.D. (2001). Cyclin-dependent kinases. *Chem Rev* *101*, 2511-2526.
- 509 Hong, C., and Tontonoz, P. (2014). Liver X receptors in lipid metabolism: opportunities for drug
510 discovery. *Nat Rev Drug Discov* *13*, 433-444.
- 511 Hu, T., Foxworthy, P., Siesky, A., Ficorilli, J.V., Gao, H., Li, S., Christe, M., Ryan, T., Cao, G.,
512 Eacho, P., et al. (2005). Hepatic peroxisomal fatty acid beta-oxidation is regulated by liver
513 X receptor alpha. *Endocrinology* *146*, 5380-5387.
- 514 Jensen, J.T., Addis, I.B., Hennebold, J.D., and Bogan, R.L. (2017). Ovarian Lipid Metabolism
515 Modulates Circulating Lipids in Premenopausal Women. *J Clin Endocrinol Metab* *102*,
516 3138-3145.
- 517 Kennedy, M.A., Venkateswaran, A., Tarr, P.T., Xenarios, I., Kudoh, J., Shimizu, N., and Edwards,
518 P.A. (2001). Characterization of the human ABCG1 gene: liver X receptor activates an
519 internal promoter that produces a novel transcript encoding an alternative form of the
520 protein. *J Biol Chem* *276*, 39438-39447.
- 521 Kersten, S., and Stienstra, R. (2017). The role and regulation of the peroxisome proliferator
522 activated receptor alpha in human liver. *Biochimie* *136*, 75-84.
- 523 Laffitte, B.A., Joseph, S.B., Walczak, R., Pei, L., Wilpitz, D.C., Collins, J.L., and Tontonoz, P.
524 (2001). Autoregulation of the human liver X receptor alpha promoter. *Mol Cell Biol* *21*,
525 7558-7568.
- 526 LaPak, K.M., and Burd, C.E. (2014). The molecular balancing act of p16(INK4a) in cancer and
527 aging. *Mol Cancer Res* *12*, 167-183.
- 528 Lee, W.H., Higuchi, H., Ikeda, S., Macke, E.L., Takimoto, T., Pattnaik, B.R., Liu, C., Chu, L.F.,
529 Siepka, S.M., Krentz, K.J., et al. (2016). Mouse Tmem135 mutation reveals a mechanism
530 involving mitochondrial dynamics that leads to age-dependent retinal pathologies. *Elife* *5*.
- 531 Lee, Y.H., Judge, A.D., Seo, D., Kitade, M., Gomez-Quiroz, L.E., Ishikawa, T., Andersen, J.B.,
532 Kim, B.K., Marquardt, J.U., Raggi, C., et al. (2011). Molecular targeting of CSN5 in human
533 hepatocellular carcinoma: a mechanism of therapeutic response. *Oncogene* *30*, 4175-
534 4184.
- 535 Masood, A., Stark, K.D., and Salem, N., Jr. (2005). A simplified and efficient method for the
536 analysis of fatty acid methyl esters suitable for large clinical studies. *J Lipid Res* *46*, 2299-
537 2305.
- 538 McAndrew, R.P., Wang, Y., Mohsen, A.W., He, M., Vockley, J., and Kim, J.J. (2008). Structural
539 basis for substrate fatty acyl chain specificity: crystal structure of human very-long-chain
540 acyl-CoA dehydrogenase. *J Biol Chem* *283*, 9435-9443.
- 541 McMullen, P.D., Bhattacharya, S., Woods, C.G., Sun, B., Yarborough, K., Ross, S.M., Miller, M.E.,
542 McBride, M.T., LeCluyse, E.L., Clewell, R.A., et al. (2014). A map of the PPARalpha
543 transcription regulatory network for primary human hepatocytes. *Chem Biol Interact* *209*,
544 14-24.
- 545 Mizuno, Y., Ninomiya, Y., Nakachi, Y., Iseki, M., Iwasa, H., Akita, M., Tsukui, T., Shimozawa, N.,
546 Ito, C., Toshimori, K., et al. (2013). Tysnd1 deficiency in mice interferes with the
547 peroxisomal localization of PTS2 enzymes, causing lipid metabolic abnormalities and
548 male infertility. *PLoS Genet* *9*, e1003286.

- 549 Newman, J.C., and Verdin, E. (2017). beta-Hydroxybutyrate: A Signaling Metabolite. *Annu Rev*
550 *Nutr* 37, 51-76.
- 551 Noland, R.C., Woodlief, T.L., Whitfield, B.R., Manning, S.M., Evans, J.R., Dudek, R.W., Lust,
552 R.M., and Cortright, R.N. (2007). Peroxisomal-mitochondrial oxidation in a rodent model
553 of obesity-associated insulin resistance. *Am J Physiol Endocrinol Metab* 293, E986-
554 E1001.
- 555 Peet, D.J., Janowski, B.A., and Mangelsdorf, D.J. (1998). The LXRs: a new class of oxysterol
556 receptors. *Curr Opin Genet Dev* 8, 571-575.
- 557 Peeters, A., Swinnen, J.V., Van Veldhoven, P.P., and Baes, M. (2011). Hepatosteatosis in
558 peroxisome deficient liver despite increased beta-oxidation capacity and impaired
559 lipogenesis. *Biochimie* 93, 1828-1838.
- 560 Repa, J.J., Liang, G., Ou, J., Bashmakov, Y., Lobaccaro, J.M., Shimomura, I., Shan, B., Brown,
561 M.S., Goldstein, J.L., and Mangelsdorf, D.J. (2000). Regulation of mouse sterol regulatory
562 element-binding protein-1c gene (SREBP-1c) by oxysterol receptors, LXRalpha and
563 LXRbeta. *Genes Dev* 14, 2819-2830.
- 564 Saini, R.K., and Keum, Y.S. (2018). Omega-3 and omega-6 polyunsaturated fatty acids: Dietary
565 sources, metabolism, and significance - A review. *Life Sci* 203, 255-267.
- 566 Salway, J.G. (1969). The simultaneous determination of acetoacetate and glucose in capillary
567 blood. *Clin Chim Acta* 25, 109-116.
- 568 Schrader, M., Godinho, L.F., Costello, J.L., and Islinger, M. (2015). The different facets of
569 organelle interplay-an overview of organelle interactions. *Front Cell Dev Biol* 3, 56.
- 570 Schwartz, D.M., and Wolins, N.E. (2007). A simple and rapid method to assay triacylglycerol in
571 cells and tissues. *J Lipid Res* 48, 2514-2520.
- 572 Seto, N.L., and Bogan, R.L. (2015). Decreased cholesterol uptake and increased liver x receptor-
573 mediated cholesterol efflux pathways during prostaglandin F2 alpha-induced and
574 spontaneous luteolysis in sheep. *Biol Reprod* 92, 128.
- 575 Stolowich, N.J., Petrescu, A.D., Huang, H., Martin, G.G., Scott, A.I., and Schroeder, F. (2002).
576 Sterol carrier protein-2: structure reveals function. *Cell Mol Life Sci* 59, 193-212.
- 577 Teboul, M., Enmark, E., Li, Q., Wikstrom, A.C., Pelto-Huikko, M., and Gustafsson, J.A. (1995).
578 OR-1, a member of the nuclear receptor superfamily that interacts with the 9-cis-retinoic
579 acid receptor. *Proc Natl Acad Sci U S A* 92, 2096-2100.
- 580 Walker, P.G. (1954). A colorimetric method for the estimation of acetoacetate. *Biochem J* 58, 699-
581 704.
- 582 Waterham, H.R., Ferdinandusse, S., and Wanders, R.J. (2016). Human disorders of peroxisome
583 metabolism and biogenesis. *Biochim Biophys Acta* 1863, 922-933.
- 584 Whitney, K.D., Watson, M.A., Goodwin, B., Galardi, C.M., Maglich, J.M., Wilson, J.G., Willson,
585 T.M., Collins, J.L., and Kliewer, S.A. (2001). Liver X receptor (LXR) regulation of the
586 LXRalpha gene in human macrophages. *J Biol Chem* 276, 43509-43515.
- 587 Wiese, S., Gronemeyer, T., Ofman, R., Kunze, M., Grou, C.P., Almeida, J.A., Eisenacher, M.,
588 Stephan, C., Hayen, H., Schollenberger, L., et al. (2007). Proteomics characterization of
589 mouse kidney peroxisomes by tandem mass spectrometry and protein correlation
590 profiling. *Mol Cell Proteomics* 6, 2045-2057.
- 591 Willy, P.J., Umesono, K., Ong, E.S., Evans, R.M., Heyman, R.A., and Mangelsdorf, D.J. (1995).
592 LXR, a nuclear receptor that defines a distinct retinoid response pathway. *Genes Dev* 9,
593 1033-1045.
- 594 Xu, Y., Hernandez-Ledezma, J.J., Hutchison, S.M., and Bogan, R.L. (2018a). The liver X
595 receptors and sterol regulatory element binding proteins alter progesterone secretion and
596 are regulated by human chorionic gonadotropin in human luteinized granulosa cells. *Mol*
597 *Cell Endocrinol* 473, 124-135.

598 Xu, Y., Hutchison, S.M., Hernandez-Ledezma, J.J., and Bogan, R.L. (2018b). Increased 27-
599 hydroxycholesterol production during luteolysis may mediate the progressive decline in
600 progesterone secretion. *Mol Hum Reprod* **24**, 2-13.
601 Yoshikawa, T., Shimano, H., Amemiya-Kudo, M., Yahagi, N., Hasty, A.H., Matsuzaka, T.,
602 Okazaki, H., Tamura, Y., Iizuka, Y., Ohashi, K., et al. (2001). Identification of liver X
603 receptor-retinoid X receptor as an activator of the sterol regulatory element-binding protein
604 1c gene promoter. *Mol Cell Biol* **21**, 2991-3000.
605 Yu, Y.P., Ding, Y., Chen, Z., Liu, S., Michalopoulos, A., Chen, R., Gulzar, Z.G., Yang, B., Cieply,
606 K.M., Luvison, A., et al. (2014). Novel fusion transcripts associate with progressive
607 prostate cancer. *Am J Pathol* **184**, 2840-2849.
608 Zarsky, V., and Dolezal, P. (2016). Evolution of the Tim17 protein family. *Biol Direct* **11**, 54.
609 Zelcer, N., Hong, C., Boyadjian, R., and Tontonoz, P. (2009). LXR regulates cholesterol uptake
610 through Idol-dependent ubiquitination of the LDL receptor. *Science* **325**, 100-104.

611 **Figure Legends**

612
613 **Figure 1: A synthetic LXR agonist induces TMEM135 expression in human hepatocyte**
614 **(HepG2, Hep3B) and monocyte-derived macrophage (THP-1) cell lines via a direct**
615 **transcriptional mechanism.** Panel A contains the results from treatment of HepG2 cells in the
616 presence or absence of the synthetic LXR agonist T09 for 6, 12, 24 and 48 hours; while panel B
617 is the effect of a 24-hour T09 treatment on *TMEM135* mRNA expression in Hep3B cells (n = 4).
618 Panel C is a time course of T09 treatment in THP-1 cells (n = 4). For panels A-C, asterisks denote
619 significant (p < 0.05) difference between DMSO and T09 at the indicated timepoint. Panel D is the
620 effect of the protein synthesis inhibitor cycloheximide on *TMEM135* mRNA expression in THP-1
621 cells. Cells were treated for 24 hours in a 2 × 2 factorial with T09 and cycloheximide (n = 5).
622 Columns with different letters are significantly different (p < 0.05). Panel E is Western blot analysis
623 of TMEM135 protein in the mitochondria/peroxisome-enriched fraction of HepG2 cells treated with
624 or without T09 for 24 hours (n = 4). The approximate molecular weights of the protein ladder are
625 indicated, as well as the TMEM135 and COX4I1 (housekeeping control) bands. Panel F is results
626 of densitometry analysis of the blot shown in Panel E, asterisk denotes significant difference (p <
627 0.05). For all panels, error bars indicate ± one standard error of the mean (SEM).

628 **Figure 2: The LXRs bind all three potential LXREs in the human TMEM135 promoter with**
629 **LXRE3 mediating LXR-induced TMEM135 transcription.** Panel A is an EMSA using LXRE1 as
630 the fluorescent probe. The nuclear receptor(s) used in the reaction are indicated beneath the

631 image, with the unlabeled competitor DNA (200-fold molar excess) shown above the image. Panel
632 B substitutes NR1H2 for NR1H3 in the binding reactions. Panel C utilizes fluorescent LXRE3 as
633 the probe. The image has been cropped to only show the bound and free fluorescent LXRE3
634 probe. The nuclear receptor(s) used in the reaction are indicated beneath the image. Increasing
635 amounts (0.25, 0.5, 1, 2, and 10-fold molar excess per competitor) of unlabeled LXRE1 or LXRE3
636 were included in some reactions as indicated above the images. In Panel D, an EMSA was
637 performed using a mixture of LXRE1 and LXRE3 probes that were labeled with spectrally-distinct
638 fluorescent dyes, as well as increasing quantities of LXR/RXR proteins. The percent of each probe
639 bound in each reaction was determined by densitometry and plotted. Panel E displays luciferase
640 activity (arbitrary units normalized to β -galactosidase) derived from cells transfected with the
641 empty vector or the *TMEM135* promoter-containing construct in the presence and absence of
642 T09. The effect of increased expression of NR1H3 and RXRA is also shown (n = 4). Panel F
643 contains the fold-increase in luciferase activity induced by T09 from the wild type *TMEM135*
644 promoter, as well as *TMEM135* promoters containing all possible combinations of mutant LXRE
645 sites (n = 4). All transfections in Panel F included *NR1H3* and *RXRA* co-transfection to increase
646 basal expression of these nuclear receptors. An X indicates point mutations were introduced into
647 the corresponding LXRE (see Figure S1), Luc = luciferase. Error bars indicate one SEM, columns
648 without common letters are significantly (p < 0.05) different. See also Figures S1 and S2.

649 **Figure 3: The LXRs are obligatory for LXR agonist-induced *TMEM135* mRNA expression,**
650 **and cause transcription of *TMEM135* with an abbreviated 5' UTR.** Panels A, B, C, and D show
651 the effects of siRNA transfection in HepG2 cells on T09-induced mRNA expression of the LXR
652 isoforms *NR1H2* and *NR1H3*, *ABCA1*, and *TMEM135*; respectively. Panel E shows the effect of
653 LXR knockdown in HepG2 cells on T09-induced expression of *TMEM135* mRNA transcripts
654 containing the full 5' UTR. Primers and probe used for QPCR in panel E amplify a 76 bp region
655 within the 5' UTR that encompasses the LXR binding site in genomic DNA. Panel F is results from

656 CHIP analysis. For all panels, error bars indicate one SEM, columns without common letters are
657 significantly ($p < 0.05$) different ($n = 4$).

658 **Figure 4: TMEM135 regulates fatty acid metabolism and proliferation of HepG2 cells.** Panel
659 A displays the effect of TMEM135 knockdown in the presence and absence of the lipogenic LXR
660 agonist T09 on intracellular triglyceride accumulation in HepG2 cells. Panel B is mRNA
661 expression in HepG2 cells for *TMEM135*, genes involved in fatty acid oxidation (*PPARA*, *CPT1A*),
662 and genes involved in fatty acid synthesis (*SREBF1*, *FASN*). For panels A and B, columns without
663 a common letter are significantly ($p < 0.05$) different ($n = 4$). Panel C is the effect of TMEM135
664 knockdown on ATP content (normalized to total protein content) in HepG2 cells after a 4-hour
665 incubation in glucose-free, sodium pyruvate-free media. The chart is plotted with the control
666 siRNA set to 1, and the asterisk denotes a significant difference ($n = 4$). Panel D is the effect of
667 TMEM135 knockdown on proliferation of HepG2 cells. Asterisks denote significant difference at
668 the corresponding timepoint ($n = 4$). Panel E is the effect of TMEM135 knockdown on cell cycle
669 progression in HepG2 cells, and panel F is the effect on mRNA expression of cell cycle-associated
670 genes. For panels E-F, asterisks denote significant differences due to TMEM135 knockdown (n
671 = 4).

672 **Figure 5: Liver-specific knockdown of TMEM135 inhibits peroxisomal β -oxidation.** Panel A
673 is mRNA expression of *Tmem135* in the listed tissues isolated from fed mice ($n = 5$). Panel B
674 displays TMEM135 protein expression in the mitochondria/peroxisome-enriched fraction from
675 livers. The right half of the image was incubated with antibody pre-absorbed with the immunizing
676 peptide. The sample contained in each lane is indicated beneath the images: MW = molecular
677 weight marker, Con = control siRNA, KD = Knockdown, *Tmem135* siRNA. The chart in panel B
678 displays the results of densitometry analysis of all 3 TMEM135 bands in the
679 mitochondria/peroxisome-enriched fraction of mice liver (fed and fasted animals pooled, $n = 10$
680 mice), as well as spectral counts from one peptide identified via proteomic analysis that was
681 mapped to TMEM135 ($n = 3$, fed animals only). In Panels A-B, asterisks denote significant

682 difference due to *Tmem135* siRNA. Panel C displays the change in body weight of animals from
683 the time of siRNA injection until sacrifice 4 days later (n = 5). Panel D displays hepatic mRNA
684 expression of *Tmem135* and genes involved in fatty acid oxidation, panel E displays hepatic NAD
685 concentrations, and Panel F is hepatic ketone concentrations (total ketones = β -hydroxybutyrate
686 + acetoacetate). For panels C-F, asterisks denote significant difference (p< 0.05) due to
687 *Tmem135* siRNA within feeding status, and # indicates significant difference due to fasting in
688 animals receiving control siRNA (n = 5). See also Figures S3 and S4.

689 **Figure 6: TMEM135 mediates import of peroxisome matrix enzymes.** Panel A displays the
690 relative purity of the mitochondria/peroxisome-enriched fraction used for proteomic analysis as
691 determined by Western blot analysis of controls for mitochondria (COX4I1), peroxisome (ABCD3),
692 and cytosolic (TUBB) proteins. For each image, the lanes from left to right are the molecular
693 weight marker (MW), whole cell lysate (WC), cytosolic fraction (Cyto), and the
694 mitochondria/peroxisome-enriched fraction (M/P). Panel B are proteins significantly decreased
695 (Fisher's Exact Test, p< 0.05) in the mitochondria/peroxisome-enriched fraction from TMEM135
696 knockdown livers, as well as the respective mean \pm SEM of their spectral counts (n = 3, fed mice
697 only). Panel C illustrates peroxisomal β -oxidation of very-long chain fatty acids (VLCFA) and
698 dicarboxylic acids (DCA). VLCFA and DCA are transported into peroxisomes via ABCDs (ABCD
699 members 1-3). Panel D illustrates peroxisomal bile acid synthesis and β -oxidation of branched
700 chain fatty acids (BCFA). Bile acid intermediates (BAI) and BCFA are transported into
701 peroxisomes via the ABCD proteins. CA = cholic acid, CDCA = chenodeoxycholic acid, BrAcyl-
702 CoA = branched chain acyl-CoA. For panels C-D, the enzymes catalyzing each step are shown
703 in boxes, and enzymes that were significantly less abundant in the mitochondria/peroxisome-
704 enriched fraction from TMEM135 knockdown mice (Panel B) are shaded. Panel E displays relative
705 peroxisome content in the mitochondria/peroxisome-enriched fractions as determined by
706 proteomic and Western blot analysis. For proteomics, only fed mice were analyzed (n = 3). For
707 Western blot, the ABCD3:COX4I1 ratio in the mitochondria/peroxisome-enriched fraction is

708 shown (n = 5). Panel F is subcellular distribution of ACAA1, ACOX1, SCP2, and CAT. ACOX1
709 migrates in 2 separate bands in Western blot, with the smaller band being proteolytically
710 processed ACOX1 (Mizuno et al., 2013). Furthermore, SCP2 (also known as SCPx) is a 58 kDa
711 protein that contains a 45 kDa 3-ketoacyl CoA thiolase domain and a 13 kDa sterol-carrier domain
712 (Stolowich et al., 2002), which are separated by proteolytic cleavage (Mizuno et al., 2013). The
713 antibody used in the current study recognizes the full-length 58 kDa protein (indicated by arrow)
714 and the 45 kDa 3-ketoacyl CoA thiolase domain, but not the 13 kDa sterol-carrier domain. The
715 identity of the other bands in the SCP2 blot is not known.

716 **Figure 7: Reduced peroxisomal import of matrix enzymes impairs β -oxidation.** Panel A
717 contains images from Western blot analysis of whole cell and mitochondria/peroxisome-enriched
718 fractions (Mito/Perox-Enriched Fraction) in livers of fed and fasted mice. Loading controls were
719 TUBB for whole cell lysates, COX4I1 for mitochondria, and ABCD3 for peroxisomes. The siRNA
720 treatment is indicated beneath the lanes, Con = control siRNA, KD = Knockdown, *Tmem135*
721 siRNA. For SCP2, the band used for densitometry analysis is indicated by asterisks. Panel B
722 displays the results of densitometry analysis of the blots shown in Panel A. Peroxisome import
723 was determined by first normalizing each protein in the mitochondria/peroxisome-enriched
724 fraction to ABCD3 to account for differences in peroxisome content, and the ratio relative to the
725 whole cell lysate (normalized to TUBB) was used to determine peroxisome import. Panel C plots
726 concentrations of C18 fatty acids quantified by GC. In panels B-C, asterisks denote significant
727 difference ($p < 0.05$) within feeding status due to *Tmem135* siRNA, and # indicates significant
728 difference due to fasting in mice receiving the control siRNA (n = 5). Panel D displays the mean
729 \pm SEM for all fatty acids (μg fatty acid per mg protein) quantified by GC. In the P column, asterisks
730 denote significant difference ($p < 0.05$) and ^ denotes trends ($0.05 < p < 0.1$) within feeding status
731 due to *Tmem135* siRNA. In the fasted mice control siRNA column, # indicates significant ($p < 0.05$)
732 difference due to fasting in control siRNA mice. See also Figure S5.

733 **STAR Methods**

734 CONTACT FOR REAGENT AND RESOURCE SHARING

735 Further information and requests for resources and reagents should be directed to and
736 will be fulfilled by the Lead Contact, Randy L. Bogan (boganr@email.arizona.edu). Transfer of
737 resources is subject to the acceptance of a Material Transfer Agreement as required by policy at
738 the University of Arizona. Resources are transferred and distributed by several means according
739 to the needs of the end-user. For other academic and non-profit researchers, the resources are
740 typically transferred under standard Material Transfer Agreements. For requests by for-profit
741 organizations, the resources are made available under standard non-exclusive license.

742 EXPERIMENTAL MODEL AND SUBJECT DETAILS

743 Cell Lines

744 All cell lines were obtained from American Type Culture Collection (ATCC) and were
745 cultured at 37°C, 5% CO₂ in air, in a humidified incubator. Human cells (all derived from males)
746 included the hepatocyte lines HepG2 (ATCC® HB-8065™) and Hep 3B2.1-7 [Hep3B] (ATCC® HB-
747 8064™), and the monocyte line THP-1 (ATCC® TIB-202™). Murine cells included the hepatocyte
748 line (embryonic-derived) BNL 1NG A.2 (ATCC® TIB-76™) and the macrophage line (male) RAW
749 264.7 (ATCC® TIB-71™). Growth media for all cell lines except THP-1 was DMEM/F12 (Sigma
750 Aldrich, Inc.) supplemented with Pen/Strep (100 units/ml penicillin and 100 µg/ml streptomycin)
751 and 10% fetal bovine serum (FBS). THP-1 cells were incubated in RPMI media (Sigma)
752 supplemented with 2-mercaptoethanol (0.05 mM), Pen/Strep, and 10% FBS. THP-1 cells were
753 differentiated into macrophages by treatment with 12-myristate-13-acetate (PMA, 100 ng/ml) for
754 5 days prior to experimentation.

755 Mice

756 All procedures involving mice were approved by the University of Arizona IACUC. Male
757 C57BL/6 mice, 12 weeks of age, were used. Mice were group housed until initiation of
758 experimental procedures, at which point they were switched to individual caging.

759 METHOD DETAILS

760 Cell Treatments

761 T0901317 (Cayman Chemical, Inc.) was dissolved in DMSO and used at a 1 μ M
762 concentration unless indicated otherwise. Cycloheximide (ACROS Organics, Inc.) was dissolved
763 in DMSO and used at a final concentration of 50 μ g/ml. The final DMSO concentration was held
764 constant in all groups at less than 0.2% (v:v). For siRNA knockdown experiments, Silencer[®] select
765 pre-designed siRNAs (Life Technologies, Inc.) against human *NR1H2* (s14684), *NR1H3*
766 (s19568), *TMEM135* (s35201), and a negative control siRNA (catalog 4390843) were purchased
767 and transfected into HepG2 cells using Lipofectamine[®] RNAiMAX (Life Technologies) or TransIT-
768 siQuest[®] reagent (Mirus Bio, LLC.) according to manufacturer instructions. All experiments were
769 repeated 4-5 times on different days or with different passages of cells.

770 HepG2 Mitochondria/Peroxisome-Enriched Fraction Isolation

771 Cells were harvested and washed three times in 1 ml cell resuspension buffer (1 mM Tris-
772 HCl, pH 7.4, 130 mM NaCl, 5 mM KCl, 7.5 mM MgCl₂). Cells were then resuspended in 600 μ l
773 homogenization buffer (10 mM Tris-HCl, pH 7.4, 10 mM KCl, 0.15 mM MgCl₂, plus protease and
774 phosphatase inhibitor cocktail), incubated on ice for 10 min, and homogenized for 30 strokes in a
775 glass dounce homogenizer with a tight-fitting pestle. The homogenate was mixed with 100 μ l of
776 2M sucrose and centrifuged at 1,200 \times g for 5 min at 4° C, and the supernatant transferred to a
777 new tube. This low speed centrifugation step was repeated two more times. Mitochondria and
778 peroxisomes were pelleted by centrifugation at 7,000 \times g for 10 min at 4° C and the supernatant
779 removed. The pellet was washed once with 300 μ l of wash buffer (10 mM Tris-HCl, pH 7.4, 0.15
780 mM MgCl₂, 250 mM sucrose), and centrifuged at 9,500 \times g for 5 min. Pellets were solubilized in
781 RIPA buffer containing protease and phosphatase inhibitors, and protein concentration was
782 determined by BCA assay (Fisher Scientific) following manufacturer recommendations.

783 Electrophoretic Mobility-Shift Analysis (EMSA)

784 The DNA sequences for human *NR1H2*, *NR1H3*, and RXR α (*RXR α*) were synthesized
785 by Life Technologies and cloned into the pTarget[™] mammalian expression vector (Promega

786 Corporation) using XhoI and KpnI restriction enzyme sites. Inserts were confirmed by DNA
787 sequence analysis. Recombinant NR1H2, NR1H3, and RXRA proteins were produced using the
788 TNT[®] Quick Coupled Transcription/Translation System (Promega). Fluorescent probes were
789 synthesized by Integrated DNA Technologies and corresponded to the LXRE1 sequence with
790 IRDye 700 attached to the 5' end, and probes corresponding to the LXRE3 sequence were
791 labelled with IRDye 800. Additionally, unlabeled DNA oligos corresponding to LXREs 1-3, as well
792 as mutated LXREs 1-3, were synthesized (Figure S1B). Single stranded DNA oligos were
793 annealed by mixing sense and antisense oligos in a 1:1 molar ratio, heating to 100°C for 5
794 minutes, and slowly cooling to room temperature. The EMSA binding reactions were carried out
795 for 30 min at room temperature in 10 mM Tris, 50 mM KCl, pH 7.5; 3.5 mM DTT, 0.25% Tween-
796 20, 1 µg Poly (dI.dC), 5 nM fluorescent probe (1 nM each for LXRE1/LXRE3 competition
797 experiment), and 1.5 µl of TNT lysate per protein (non-induced TNT lysate substituted in control
798 reactions). Unlabeled competitor DNA was added prior to the addition of fluorescent probe at a
799 200-fold molar excess unless indicated otherwise. Following the incubation period, EMSA
800 reactions were resolved on a 6% TBE gel (Life Technologies). Imaging and densitometry were
801 performed with a Li-COR Odyssey CLx and Image Studio version 3.1 software, respectively.

802 Reporter Assays

803 The region from -2662 to -1 bp (relative to translation start site) of the human *TMEM135*
804 promoter was synthesized by Life Technologies. Additionally, the same region of the human
805 *TMEM135* promoter was synthesized except that point mutations were introduced into each of
806 the three LXREs (Figure S1B). The normal and mutant *TMEM135* promoters were cloned into the
807 pGL4.17 vector (Promega) using SacI and XhoI restriction enzyme sites, which expresses firefly
808 luciferase from a promoter cloned into the vector. A unique PacI site was identified in the region
809 between LXRE1 and LXRE2, and a unique EcoRI site was identified in the region between LXRE2
810 and LXRE3. These restriction sites were used to generate six more *TMEM135* promoter/pGL4.17
811 constructs so that all possible combinations of wild type and mutated LXREs were obtained. All

812 constructs were verified using DNA sequence analysis. These reporter vectors were transfected
813 into HepG2 cells along with a β -galactosidase control plasmid (Promega) to normalize
814 transfection efficiency. In some transfections, *NR1H3*/pTarget and *RXRA*/pTarget constructs
815 were co-transfected. Vectors were transfected in a ratio of 60:20:10:10 (luciferase: β -
816 galactosidase:NR1H3:RXRA) using Lipofectamine[®] 3000 according to manufacturer
817 recommendations, with no-insert plasmids substituted in control transfections to keep DNA
818 concentrations constant. Each vector combination was transfected in triplicate to HepG2 cells in
819 96 well plates, and cells were incubated with DNA/Lipofectamine complexes for 24 hours at which
820 point media were changed and cells were treated for an additional 48 hours with DMSO or T09.
821 Cell lysates were prepared using mammalian protein extraction reagent (Fisher), and the lysate
822 was fractionated to quantify luciferase and β -galactosidase activity using luminescent detection
823 kits (Fisher). The ratio of luciferase to β -galactosidase activity was calculated, and the fold-change
824 in T09 vs DMSO treated cells was determined for each transfection.

825 Chromatin Immunoprecipitation (ChIP) Analysis

826 HepG2 cells were fixed for 10 min at room temperature with 1% formaldehyde. The
827 reaction was quenched by adding glycine to a 125 mM final concentration and incubating 5 min
828 at room temperature. The cells were trypsinized, harvested, and washed twice with PBS. Nuclei
829 were isolated by incubating cell pellets in 500 μ l of a hypotonic buffer for 15 min on ice (20 mM
830 Tris-HCL, pH 7.4, 10 mM NaCl, 3 mM MgCl₂, with protease and phosphatase inhibitor cocktail
831 from Promega). Triton X-100 detergent was added to a 0.5% v:v final concentration to lyse the
832 cells followed by centrifugation at 1200 \times g for 10 min to pellet nuclei. The supernatant was
833 removed, and the nuclei pellet washed once with 500 μ l hypotonic buffer. The pellet was
834 resuspended in 500 μ l of RIPA buffer with protease and phosphatase inhibitors, and nuclei were
835 sonicated in an ice-water bath using a Branson 250 digital sonifier programmed to cycle at a 10%
836 amplitude with 5 seconds on followed by 20 seconds off, and a 3-minute total sonication time that
837 was determined in preliminary time-course studies to produce chromatin of optimal length

838 (approximately 200-1000 base pairs). The sonicated lysates were centrifuged at 8,000 × g for 1
839 minute and the supernatant recovered. An aliquot of cleared lysate was treated with 25 µg RNase
840 A and 50 µg proteinase K in a buffer containing 500 mM NaCl and heated at 65°C for 1.5 hours
841 to reverse cross-links. The DNA concentration in this aliquot was determined using a fluorometric
842 assay (Life Technologies) following manufacturer recommendations. The quantity of DNA used
843 in each ChIP was held constant within replicates (8 to 10 µg), and 10% of the input amount was
844 saved. Chromatin was diluted to a 500 µl final volume in binding/wash buffer (50 mM Tris, 150
845 mM NaCl, 1% Triton X-100) containing protease and phosphatase inhibitors, and 3 µg of antibody
846 was added per reaction. Tubes were incubated on an end-over-end rotator at 4°C overnight.
847 Antibodies used for ChIP were mouse monoclonal IgG2a including: 1) anti-NR1H3 (clone
848 PPZ0412, R&D Systems catalog PP-PPZ0412-00), 2) anti NR1H2 (clone K8917, R&D Systems
849 catalog PP-K8917-00), and 3) non-specific control IgG2a (clone MOPC-173, Abcam catalog
850 ab18413). The following day 25 µl of Protein G-conjugated Dynabeads (Life Technologies) were
851 added and incubated for 1 hour at 4°C. The beads were recovered using a magnet and washed
852 three times at 4°C for 5 minutes each wash with 1 ml of binding/wash buffer. The beads were
853 then washed once in final wash buffer (50mM Tris, 500 mM NaCl, 1% Triton X-100). Elutions
854 were performed with 130 µl elution buffer (100mM NaHCO₃, 500mM NaCl, 1% SDS) containing
855 25 µg RNase A and 50 µg proteinase K, and ChIP reactions and input controls were incubated
856 on a thermal mixer at 65°C for 1.5 hours. The supernatant was recovered, and DNA purified using
857 PCR purification columns (Life Technologies) following manufacturer recommendations. Purified
858 DNA was analyzed by QPCR in a duplex reaction with primers and a Taqman probe specific for
859 the region spanning LXRE3 on the *TMEM135* gene, and a non-specific locus was simultaneously
860 quantified in the same reaction as a control for non-specific DNA carryover (Table S1). Serial
861 dilutions of purified sonicated DNA were included to verify linear amplification and PCR efficiency,
862 and Ct values from ChIP reactions and input controls were used to calculate the percentage of

863 DNA recovered relative to the input. Data were normalized by calculating the ratio of the
864 TMEM135 LXRE3 to the non-specific chromatin locus.

865 Semi-Quantitative Real-Time PCR

866 Cells or tissue were homogenized in Trizol reagent for isolation of mRNA and were further
867 purified over RNeasy columns according to manufacturer recommendations (Life Technologies).
868 Concentrations of RNA were quantified by spectrophotometry, and 0.2-1 µg RNA was treated with
869 DNase I and reverse transcribed into cDNA using the High Capacity cDNA Reverse Transcription
870 Kit (Life Technologies). Following reverse transcription, cDNA were diluted to 10 ng/µl (based on
871 original RNA concentration) and used for semi-quantitative real-time PCR analysis (QPCR).
872 Primer and probe sequences used for QPCR are listed in Table S1. The QPCR assays were
873 performed on a StepOne Plus Real-Time PCR system (Life Technologies) using TaqMan® MGB
874 probe or SYBR green detection. Relative mRNA abundance was determined by extrapolation of
875 threshold (Ct) values from a standard curve of serial cDNA dilutions and normalized to the
876 housekeeping gene mitochondrial ribosomal protein S10 (*MRPS10*).

877 Cell Proliferation Assay

878 HepG2 cells were plated at 15,000 cells per well in 96-well plates and transfected with
879 siRNAs immediately. At the appropriate post-transfection time, viable cells were quantified using
880 a CyQuant® Direct Cell Proliferation assay (Life Technologies) according to manufacturer
881 recommendations, and fluorescence (excitation 495 nm, emission 527 nm) determined using a
882 Synergy H1 plate reader (BioTek Instruments, Inc.) in area scanning mode to account for uneven
883 cell distribution. The number of cells per well was estimated by extrapolation from a standard
884 curve of increasing cell numbers that was generated at the time of plating.

885 Flow Cytometry Analysis of Cell Cycle

886 Freshly harvested HepG2 cell pellets were fixed by slow addition of 1 ml ice-cold 70%
887 ethanol while vortexing and incubated at -20°C overnight. Fixed cells were harvested by
888 centrifugation at 850 × g for 5 min and resuspended in 1 ml DNA staining buffer (100 µg/ml RNase

889 A, 50 µg/ml propidium iodide, in PBS). Cells were incubated for 30 min at 37°C, placed on ice,
890 and analyzed within one hour. A Becton Dickinson FACSCANTO II flow cytometer equipped with
891 a 488 nm argon ion laser and a 585/42 bandpass filter was used for detection of bound propidium
892 iodide. List mode data files consisting of 10,000 events were acquired and the percentage of cells
893 in G0/G1, S, and G2/M stages was determined with CellQuest PRO software (BD Biosciences).

894 HepG2 ATP Quantification

895 At 48 hours post-siRNA transfection, HepG2 cells were switched to serum-free, glucose-
896 free, sodium pyruvate-free DMEM media and incubated at 37°C for 4 hours. Cellular ATP
897 concentrations were determined using a homogenous luminescent ATP detection kit (Abcam
898 catalog ab113849). Additional HepG2 cells treated in parallel to those used for ATP determination
899 were lysed in RIPA buffer and a BCA protein assay (Fisher) was performed, and ATP content
900 was normalized to protein concentrations.

901 Triglyceride Quantification

902 HepG2 cells or frozen mouse liver were sonicated in PBS containing protease and
903 phosphatase inhibitors (Promega) in an ice-water bath using a Branson 250 digital sonifier
904 programmed to cycle at a 10% amplitude with 5 seconds on followed by 20 seconds off, and a 30
905 second total sonication time. Triglycerides were extracted using an organic solvent procedure
906 optimized for triglycerides (Schwartz and Wolins, 2007). Lysates were diluted 1:1 with deionized
907 water, and 400 µl of diluted lysate was combined in a glass tube with 1.8 ml of a 4:1
908 isopropanol:hexane mixture. Samples were vortexed for 1 minute and incubated at room
909 temperature for 30 min. Next, 500 µl of a 1:1 hexane:diethyl ether solution was added, the
910 samples were vortexed as before, and incubated at room temperature for 1 minute. One ml of
911 deionized water was added, samples were vortexed as before, and incubated at room
912 temperature for 20 minutes to allow phase separation. The organic phase was transferred to a
913 new glass tube and dried under a gentle stream of nitrogen in a water bath at 30°C. Dried extracts
914 were dissolved in 200 µl assay buffer (50 mM potassium phosphate, pH 7.0, 0.01% Triton X-100)

915 by 5 total cycles of vortexing for 1 minute and incubating at room temperature for 3 minutes.
916 Extracts (50 μ l/well) were transferred to a clear 96 well plate, and 250 μ l of triglyceride detection
917 reagent (Pointe Scientific, Inc., catalog T7532) was added. Triglyceride standards (Pointe
918 Scientific) diluted in assay buffer were also run with each assay. Plates were incubated at 37°C
919 for 30 minutes with vigorous shaking, and absorbance at 500 nm was determined with a Synergy
920 H1 plate reader. The protein concentration in sonicated lysates was determined using a BCA
921 protein assay, and triglyceride content was normalized to protein content.

922 In Vivo siRNA Delivery and Tissue Harvest

923 Ambion® In Vivo pre-designed siRNA (Life Technologies) against *Tmem135* (s91285) or
924 *in vivo* negative control #1 siRNA (catalog 4459405) were complexed with InvivoFectamine® 3.0
925 reagent (Life Technologies) according to manufacturer recommendations. The siRNA complexes
926 were delivered via a 200 μ l tail-vein injection at a final siRNA concentration of 1 mg/kg body
927 weight. Mice were weighed prior to siRNA injection and again before euthanization. Mice were
928 euthanized 4 days after siRNA injection at 4 hours after lights on, with or without a preceding 12
929 hour fast. Serum, liver, heart, adipose, and skeletal muscle were collected and snap frozen.
930 Tissues were powdered while frozen and stored at -80° C until used.

931 Serum Analytes

932 Total cholesterol, HDL cholesterol, and triglyceride concentrations in serum were
933 determined as we have described previously (Jensen et al., 2017). Briefly, the HDL fraction of
934 serum was isolated by mixing serum 1:1 with 15% polyethylene glycol, centrifuging at 2,000 \times g
935 for 10 minutes at room temperature, and harvesting the HDL-containing supernatant. The
936 cholesterol concentrations in whole serum and the HDL fraction were determined by a
937 fluorometric enzyme assay consisting of cholesterol esterase (0.3 units/ml), cholesterol oxidase
938 (1 unit/ml), horse radish peroxidase (1 unit/ml), and Amplex UltraRed® (50 μ M, Life Technologies)
939 in assay buffer (0.1 M potassium phosphate, pH 7.0, 50 mM NaCl, 5 mM cholic acid, 0.1% Triton
940 X-100). The cholesterol assay was incubated at 37°C for 30 minutes, and fluorescence measured

941 in a Synergy H1 plate reader at 555 nm excitation and 585 nm emission wavelengths. Triglyceride
942 concentrations in whole serum were determined using the same assay described earlier for
943 HepG2 and mouse liver samples. Commercial enzymatic assays were used to quantify serum
944 concentrations of β -hydroxybutyrate (BHB) (Cayman Chemical, catalog 700190), non-esterified
945 fatty acids (NEFA) (Catachem Inc., catalog C514-0A), glucose (Pointe Scientific, Inc., catalog
946 G7521), and a commercial ELISA was used to quantify serum insulin (Merckodia AB, catalog 10-
947 1247) according to manufacturer recommendations.

948 Liver Analytes

949 Commercial kits were used for the extraction and quantification of liver NAD⁺ and NADH
950 (Abcam Inc., catalog ab176723), and glycogen (BioAssay Systems, catalog E2GN), according to
951 manufacturer recommendations. Concentrations of ATP and NEFAs in liver were determined as
952 we have described elsewhere (Geisler et al., 2016). Briefly, for ATP determination frozen
953 powdered liver was homogenized in ATP releasing agent (Sigma Chemical Co., catalog FLSAR).
954 ATP was quantified with a luminescent ATP Determination Kit (Life Technologies, catalog
955 A22066) and normalized to tissue weight. For NEFAs, powdered liver was sonicated in PBS as
956 described earlier, and 100 μ l lysate was mixed with 1 ml of 100% ethanol. Samples were vortexed
957 for 10 minutes, centrifuged at 16,000 \times g for 5 minutes, and the supernatant recovered. A
958 commercial colorimetric assay for NEFAs (Catachem Inc., catalog C514-0A) was used and
959 standards were diluted in ethanol, and NEFA concentrations were expressed on an equal protein
960 basis.

961 To quantify ketones (BHB and acetoacetate), powdered liver was sonicated in PBS,
962 acidified with 10% (*w:v*) trichloroacetic acid, centrifuged to remove proteins, and the supernatant
963 was recovered and neutralized. Concentrations of BHB in the extract were determined using the
964 same enzymatic assay described for serum. Concentrations of acetoacetate were determined
965 using a modified assay based on methods described previously (Salway, 1969; Walker, 1954).
966 Briefly, samples and standards were divided with one portion subjected to boiling (100° C for 5

967 minutes) to degrade acetoacetate, with the remaining portion kept on ice. A three-fold volume of
968 freshly prepared diazo reagent (Walker, 1954) was then added to all samples and incubated at
969 room temperature in the dark for 30 minutes. The reaction was stopped by adding a 20% volume
970 of 2N NaOH, and absorbance was measured at 480 nm. The absorbance from the boiled sample
971 was subtracted from the respective non-boiled sample, and acetoacetate concentrations were
972 calculated from the resultant standard curve. Concentrations of cholic acid in liver were quantified
973 using a competitive enzyme immunoassay according to manufacturer recommendations (Cell
974 Biolabs, Inc., catalog MET-5007).

975 Liver Subcellular Fractionation

976 Powdered liver (approximately 50 mg) was homogenized for 40 strokes in a glass dounce
977 homogenizer with a tight-fitting pestle using 600 μ l of cold fractionation buffer (10 mM Tris-HCl,
978 pH 7.4, 1 mM EGTA, 200 mM sucrose, protease and phosphatase inhibitor cocktail) on ice. The
979 homogenate was transferred to a new tube, and the dounce homogenizer was washed with an
980 additional 600 μ l of fractionation buffer and transferred to the same tube. The homogenate was
981 centrifuged at 600 \times g for 10 minutes at 4°C to pellet unbroken cells and nuclei, and the
982 supernatant transferred to a new tube. This low speed spin was repeated once more.
983 Mitochondria and peroxisomes were pelleted by centrifugation at 7,000 \times g for 10 minutes, and
984 the supernatant (cytosolic fraction) was transferred to a new tube. The pellet was washed with
985 300 μ l fractionation buffer and pelleted as before. The pellet was resuspended in 500 μ l of
986 fractionation buffer and a 30 μ l aliquot was pelleted and solubilized in RIPA buffer for a BCA
987 protein assay. Following protein assay mitochondria/peroxisome fractions were partitioned into
988 30 μ g (protein content) aliquots followed by centrifugation and removal of the supernatant, and
989 the pellets were frozen at -80°C.

990 Proteomic Analyses

991 The mitochondria/peroxisome-enriched fraction from a subset of fed control and
992 TMEM135 knockdown mice was solubilized in RIPA buffer, proteins were precipitated with

993 acetone, and proteins were sent to the Arizona Proteomics Consortium for mass spectrometry
994 identification of proteins. Proteins were digested with trypsin and equal quantities of protein (500
995 ng) were loaded. Samples were analyzed on a Thermo Q Exactive Plus Orbitrap mass
996 spectrometer. Peptide identification in the resultant tandem mass spectra was performed using
997 Proteome Discoverer Software version 1.3.0.339 scanning with the SEQUEST algorithm against
998 the mouse proteome database (Mouse_unitprotkb_proteome_2016_0720_cont.fasta). Data
999 analysis was performed using Scaffold version 4.8.1, with a peptide identification threshold of
1000 95.0% and a minimum protein identification threshold of 99.9% and 2 unique peptides.

1001 Western Blot

1002 All primary antibodies were obtained from Abcam unless otherwise indicated. Catalog
1003 numbers and final concentrations or dilutions of each antibody were: rabbit polyclonal anti-ACAA1
1004 (catalog ab154091, 1 µg/ml), rabbit monoclonal anti-ACOX1 (catalog ab184032, 1:2500 dilution),
1005 rabbit monoclonal anti-CAT (catalog ab209211, 1:2000 dilution), rabbit monoclonal anti-SCP2
1006 (catalog ab140126, 1:2500 dilution), rabbit polyclonal anti-TMEM135 (catalog ab167096, 1
1007 µg/ml), rabbit monoclonal anti-COX4I1 (Li-COR Inc., catalog 926-42214, 1:1000 dilution), mouse
1008 monoclonal anti-COX4I1 (catalog 14744, 0.25 µg/ml), mouse monoclonal anti-TUBB (Sigma
1009 Aldrich catalog T8328, 0.5 µg/ml), and rabbit polyclonal anti-PMP70 (catalog ab3421, 0.5 µg/ml).

1010 Proteins (12.5 µg/well) were resolved on 4-12% Bis-Tris gels (Life Technologies) and
1011 subsequently transferred to nitrocellulose membranes. The membranes were blocked with 5%
1012 non-fat dry milk (NFDM) (w:v) in TBS with 0.1% (v:v) Tween (TBST) for 1 hour at room temp. All
1013 primary antibodies were diluted in TBST with 1% NFDM and incubated with the membranes on a
1014 rocking platform at 4° C overnight. The membranes were washed 4x with TBST, and IRDye®
1015 680RD or 800CW-conjugated secondary antibodies (LI-COR Biosciences, Inc.) were diluted
1016 1:4000 in TBST + 1% NFDM and incubated with membranes for 1 hour at room temp. The
1017 membranes were washed as before. Imaging and densitometry were performed with a Li-COR
1018 Odyssey CLx and Image Studio version 3.1 software, respectively.

1019 Gas Chromatography (GC)

1020 Lysates were prepared by sonicating frozen powdered liver in PBS as described earlier.
1021 Insoluble material was pelleted by centrifugation at 600 × g for 5 minutes. A BCA protein assay
1022 was performed on the cleared lysate. A one-step transesterification reaction was performed
1023 (Masood et al., 2005). Briefly, 1.7 ml of acidic methanol (1.6 ml methanol and 100 µl acetyl
1024 chloride) was added to borosilicate glass tubes with Teflon-lined caps. Butylated hydroxytoluene
1025 (BHT, 50 µg/ml) was added to methanol to prevent fatty acid oxidation. Tridecanoic acid (13:0,
1026 Cayman Chemical) was used as an internal standard because preliminary studies determined
1027 that it was not present in liver lysates. Tridecanoic acid was diluted in methanol/BHT to 100 µg/ml,
1028 and 100 µl was added to all samples and standards. Authentic standards for the following fatty
1029 acids were obtained from Cayman Chemical: 12:0, 14:0, 16:0, 16:1, 18:0, 18:1 cis(n9), 18:2
1030 cis(n6), 20:3 cis(n6), 20:4 (n6), 22:0, 22:6 (n3), 24:0, 24:1, and 26:0. Pooled mixtures containing
1031 increasing concentrations of these fatty acids were prepared and dissolved in chloroform. 100 µl
1032 of authentic standards were added to standard tubes, and 100 µl of chloroform was added to
1033 unknown tubes. Next, 100 µl PBS was added to standard tubes, and 800 µg (protein content) of
1034 lysate diluted to a 100 µl volume with PBS was added to unknown tubes. The tubes were tightly
1035 capped and vortexed for 1 minute, and then incubated in a heating block at 100°C for one hour.
1036 The tubes were cooled to room temperature, 750 µl hexane was added and the tubes were
1037 vortexed for 30 seconds, and the upper organic layer was transferred to a GC sample vial. The
1038 hexane extraction was repeated once more. Hexane extracts were evaporated under a gentle
1039 stream of nitrogen to dryness and dissolved in 50 µl hexane.

1040 GC was performed on an Agilent Technologies 6890N GC equipped with a Varian CP-Sil
1041 88 column for fatty acid methyl ester analysis (100 m × 0.25 mm inner diameter × 0.2 µm film
1042 thickness) and a flame ionization detector. Inlet temperature was 250° C, and 1 µl of each
1043 standard or unknown was manually injected at a split ratio of 7.5:1. Helium was used as carrier
1044 gas at a 1.0 ml/minute constant flow. The oven was programmed for an initial temperature of 80°

1045 C with a 4° C/min ramp to 220° C, a 5-minute hold, then a 4° C/min ramp to 240° C followed by a
1046 10-minute hold. The detector was set at 270°C using air (450 ml/minute) and hydrogen (40
1047 ml/minute), and nitrogen was used as make-up gas (10 ml/minute constant flow). The sampling
1048 frequency was 20 Hz.

1049 OpenLAB CDS ChemStation Edition software version C.01.06 (Agilent Technologies) was
1050 used to analyze GC data. Retention times of authentic standards were matched with
1051 corresponding peaks in unknown samples. For each fatty acid, the peak area for standards and
1052 unknowns was divided by the internal standard peak area. The normalized peak area from
1053 increasing concentrations of authentic standards was plotted, and the R² for the resultant standard
1054 curves were > 0.995 in all cases. All fatty acids except 12:0 and 26:0 were identified in the
1055 unknowns, and fatty acid concentrations were determined by extrapolating the normalized peak
1056 area from the respective standard curve. Concentrations were expressed on an equal protein
1057 basis.

1058 **QUANTIFICATION AND STATISTICAL ANALYSIS**

1059 Statistical analyses were performed using Stata Version 14 and all differences were
1060 considered significant at p< 0.05. Information on the sample size, mean and error estimates, and
1061 indicators of statistical significance are presented in the figures and their corresponding legends.
1062 For immortalized cell lines, the total sample size (n) corresponds to cells on a different passage
1063 number and/or experiments performed on different days. Time course data in immortalized cell
1064 lines were analyzed by mixed effects regression analysis to account for repeated measures.
1065 Treatments were coded 0 or 1, and hours post-treatment and treatment × time interaction were
1066 included as fixed effects in the regression model with experimental replicate as the random effect.
1067 Differences between treatments at each timepoint were determined from the treatment × time
1068 interaction coefficient. For all other comparisons involving more than 2 groups, mixed effects
1069 regression analysis was performed using treatment as the fixed effect and experimental replicate
1070 as the random effect to account for repeated measures. Pairwise differences between treatments

1071 were then determined using the Bonferroni multiple comparison method to control for the type 1
1072 error rate. For comparisons involving only 2 groups, a paired t-test was performed.

1073 For all mice data, the sample size refers to the number of mice. Regression analysis was
1074 used for mice outcomes except where indicated otherwise. Samples were coded 0 or 1 for fasting,
1075 TMEM135 knockdown fed mice, and TMEM135 knockdown fasted mice. The regression model
1076 utilized fasting, TMEM135 knockdown in the fed state, and TMEM135 knockdown in the fasted
1077 state, as predictors. The fasting coefficient indicated the difference due to fasting in control mice
1078 only, while the TMEM135 knockdown coefficients indicated the difference between control mice
1079 and TMEM135 knockdown mice within the fed state or fasted state. Differences were considered
1080 significant at $p < 0.05$, with p values ≥ 0.05 and < 0.10 considered trends. Only fed mice were
1081 used in proteomic analysis. Because the proteomic data does not follow a normal distribution due
1082 to some proteins not being detected in all samples, significant differences in proteomic data were
1083 determined from weighted spectra using the non-parametric Fisher's Exact test ($p < 0.05$)
1084 contained within the Scaffold version 4.8.1 software. The list of proteins that were significantly
1085 reduced in knockdown livers was further trimmed by hand to exclude proteins that were not
1086 detected in all the samples from mice that received the control siRNA.

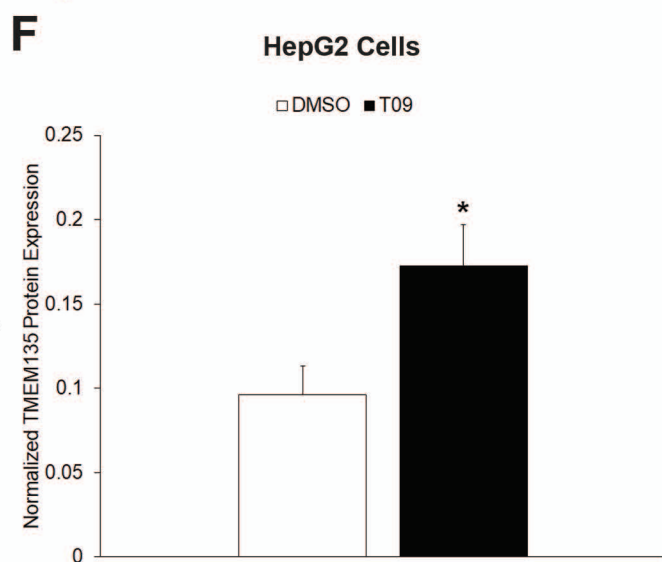
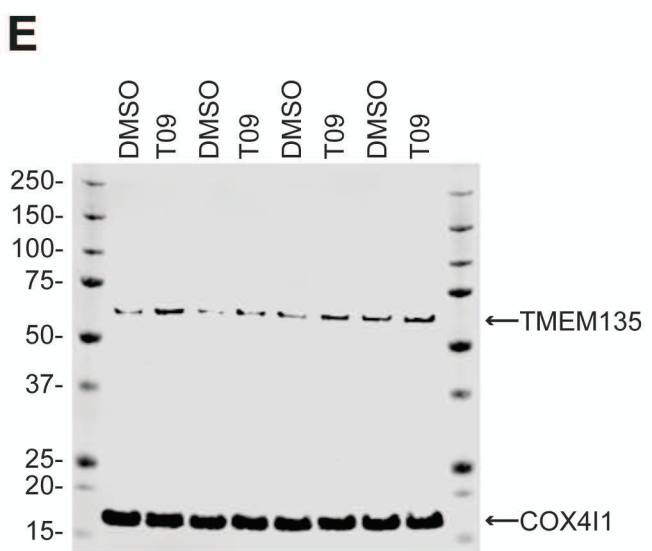
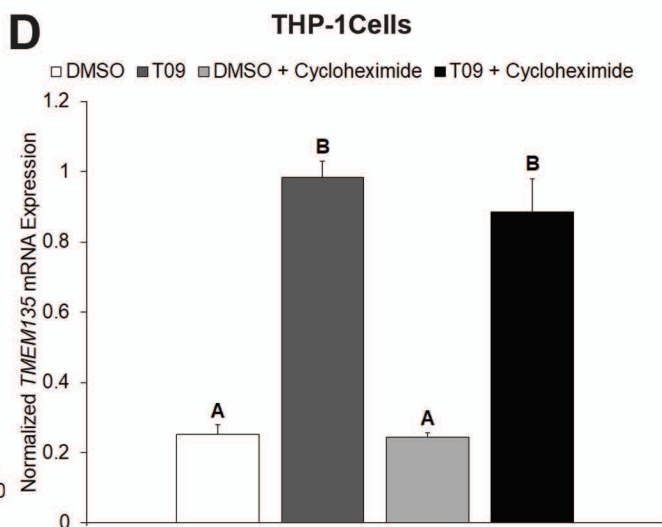
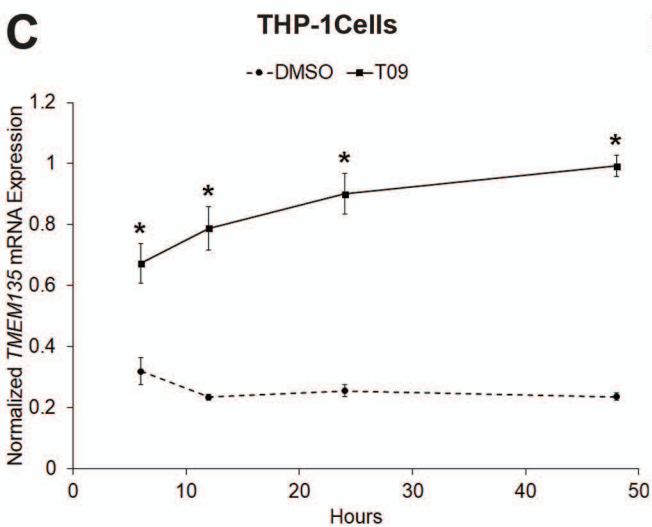
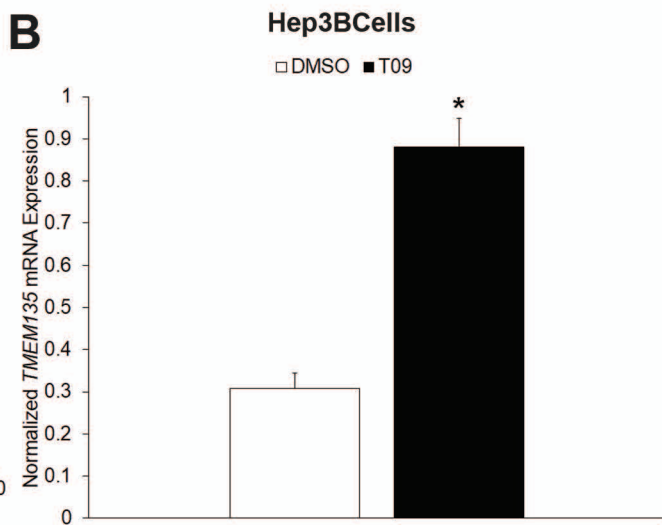
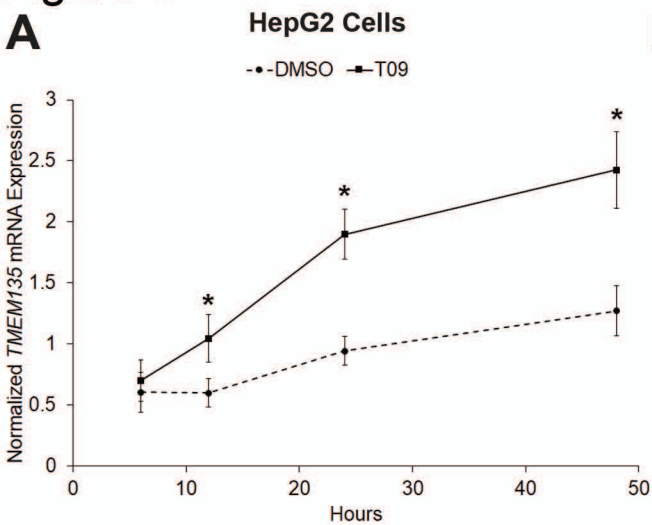
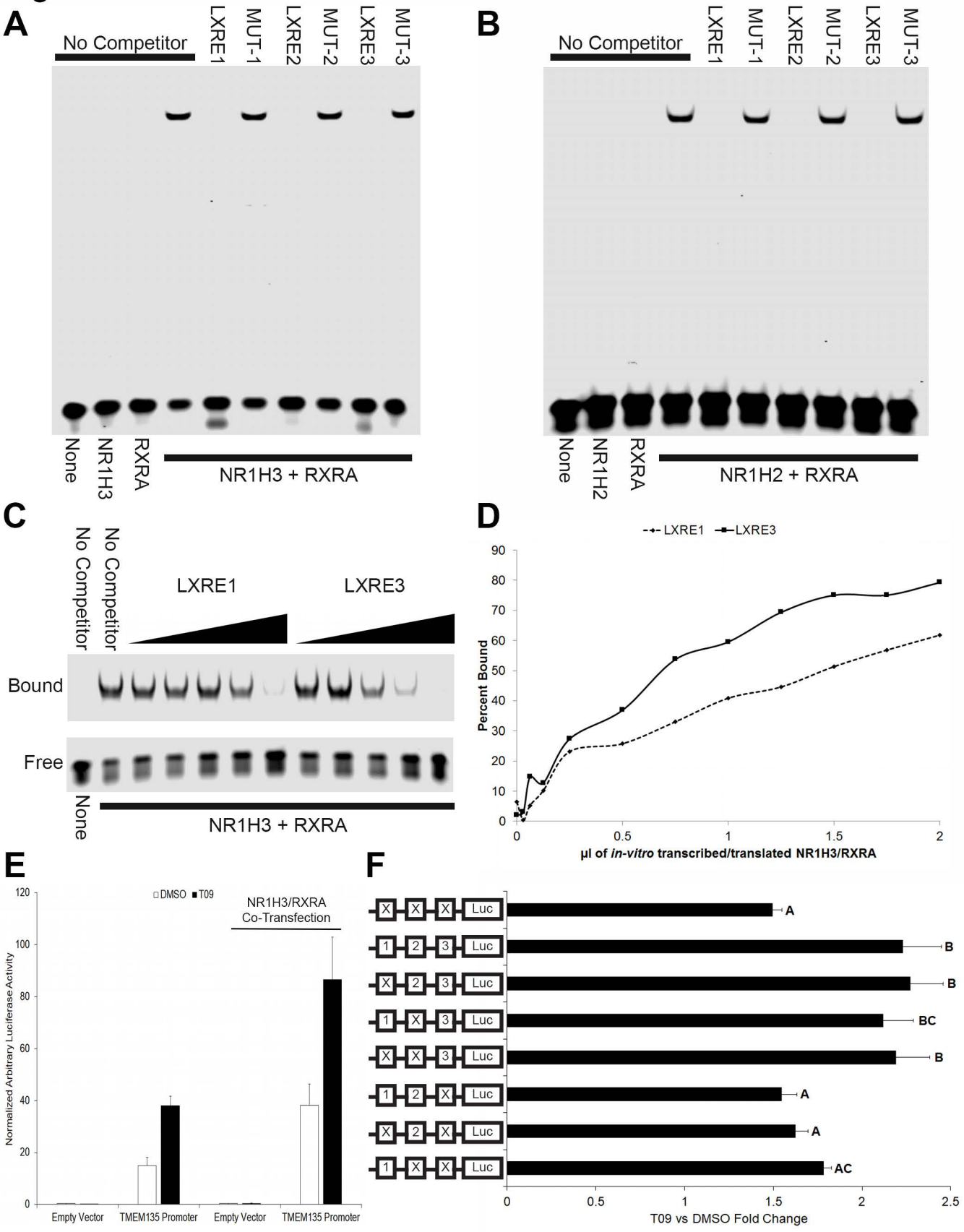
Figure 1

Figure 2



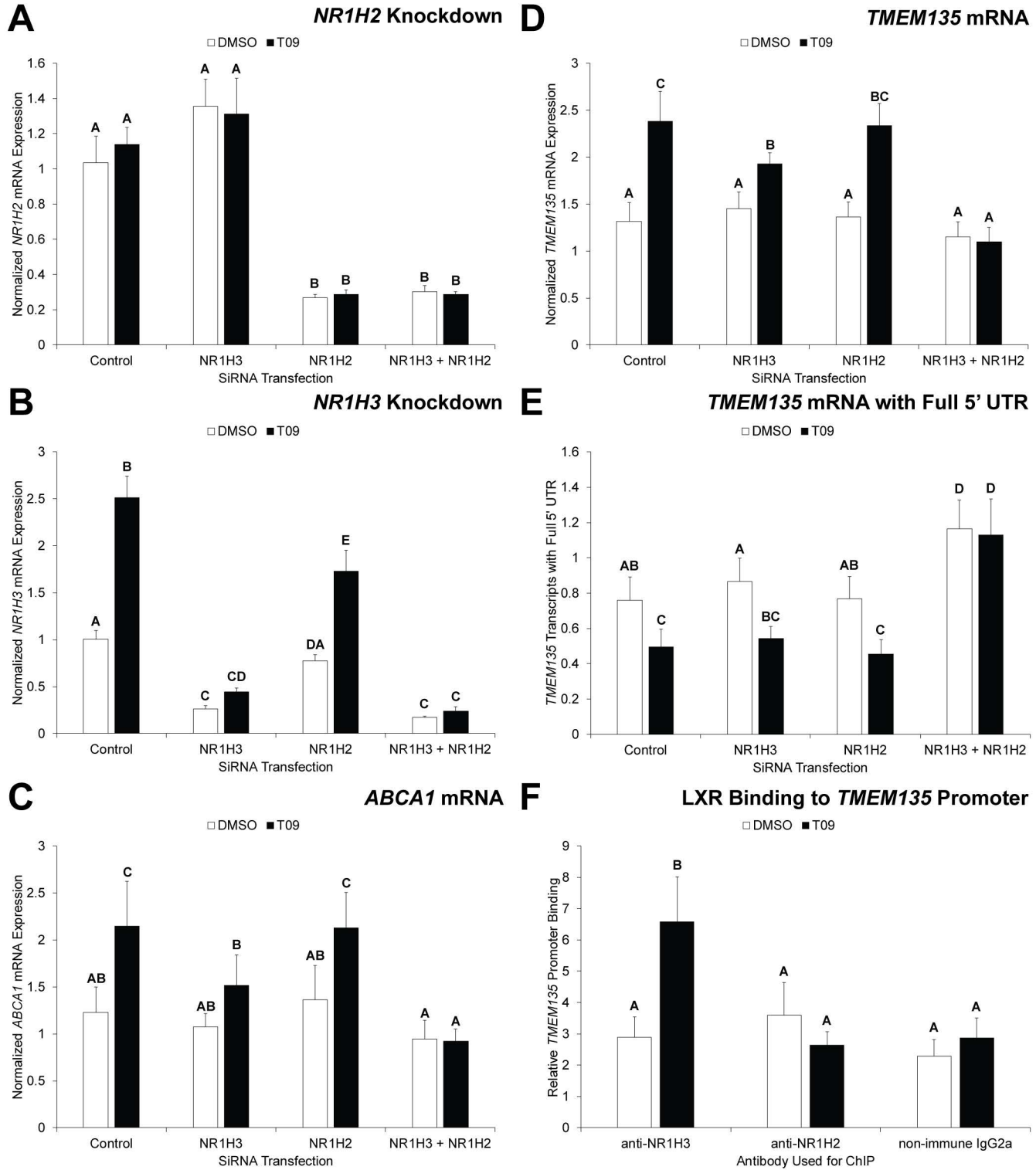


Figure 3

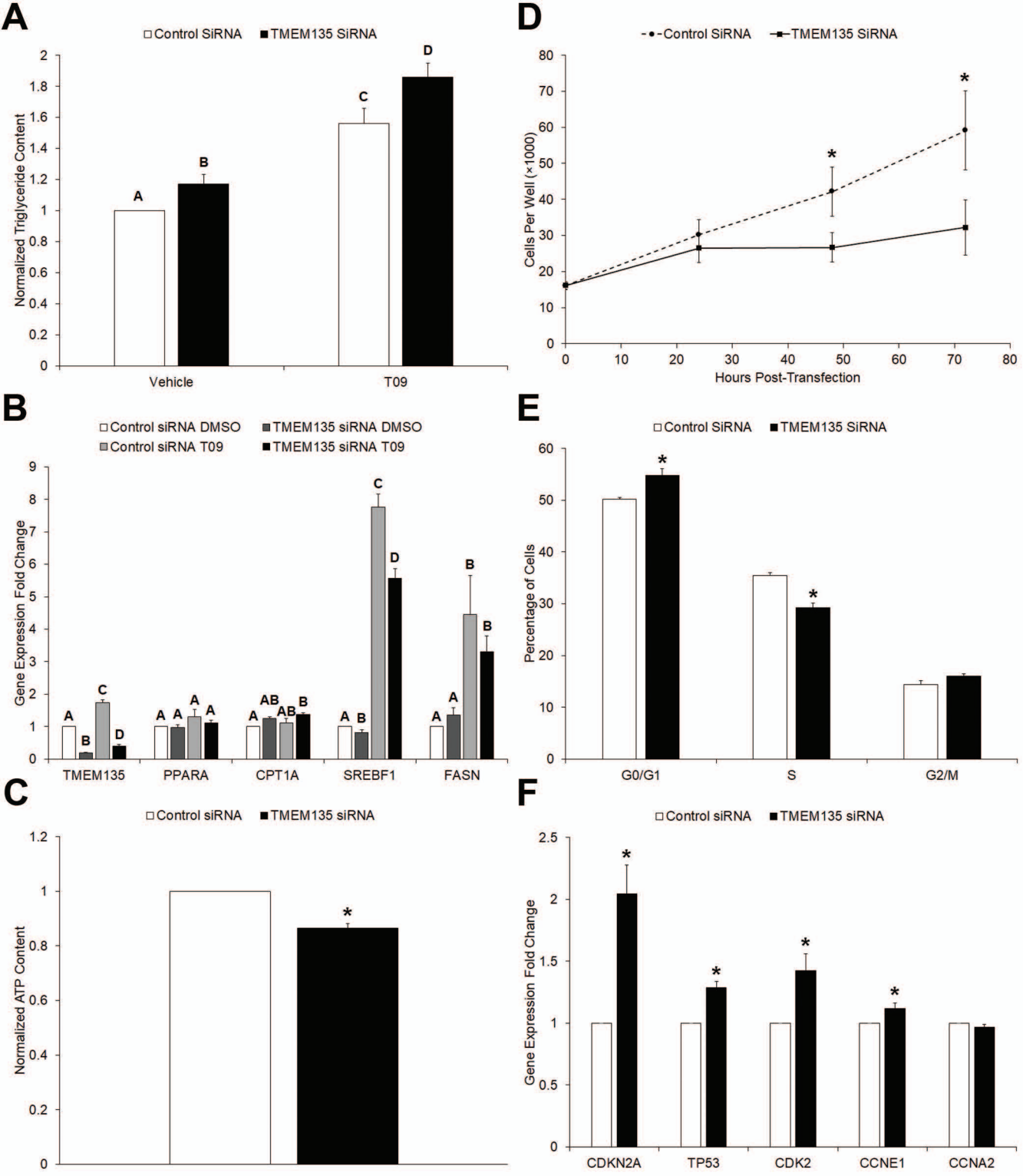


Figure 4

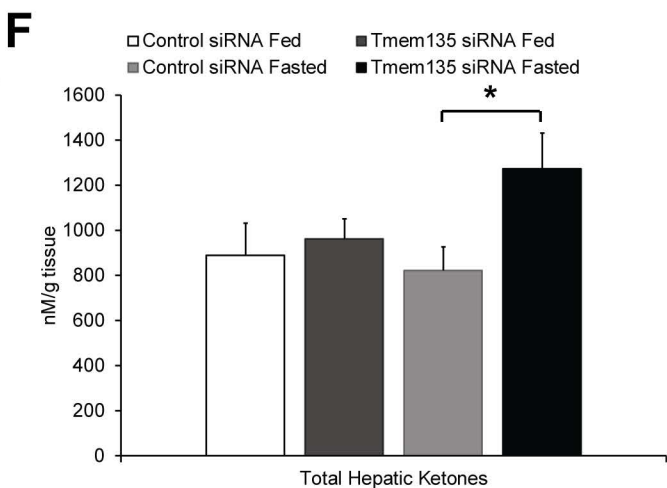
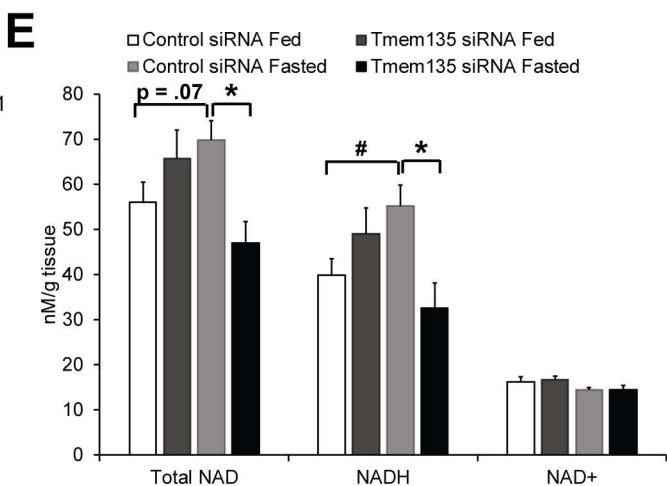
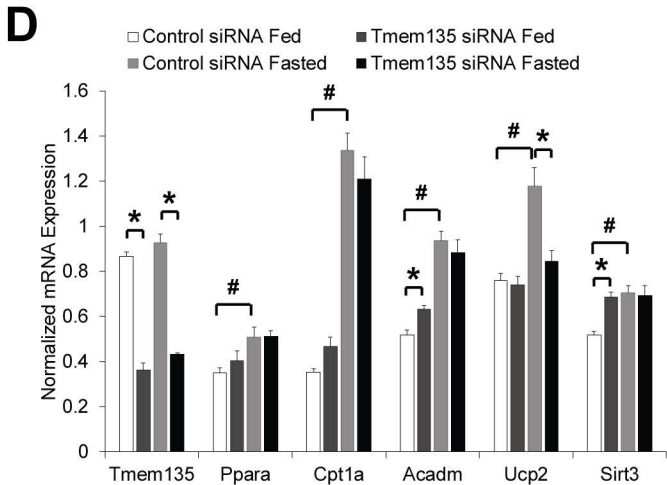
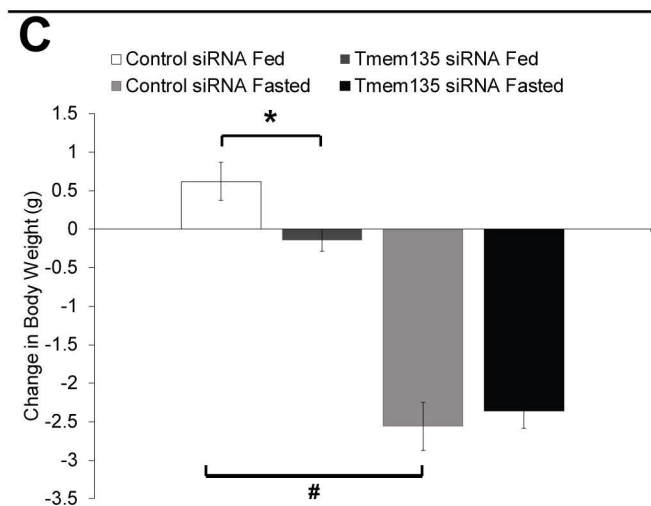
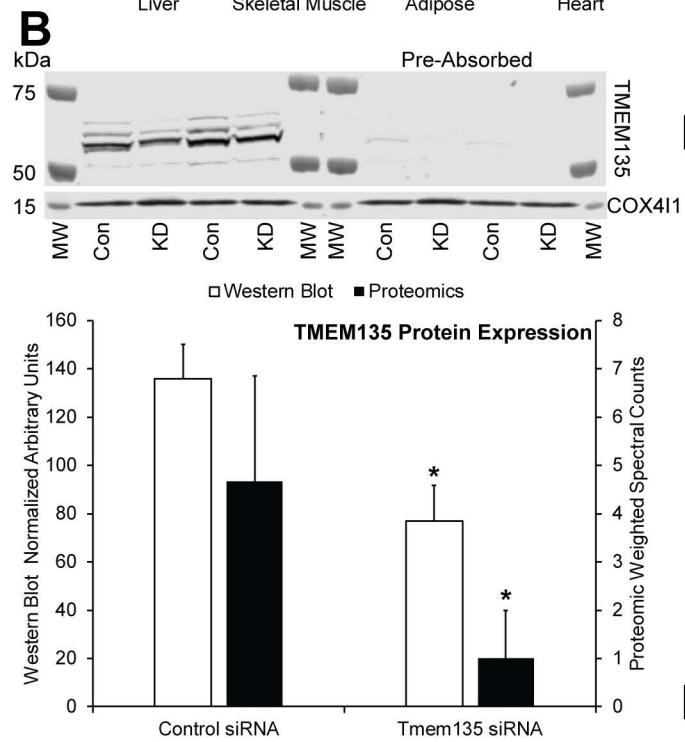
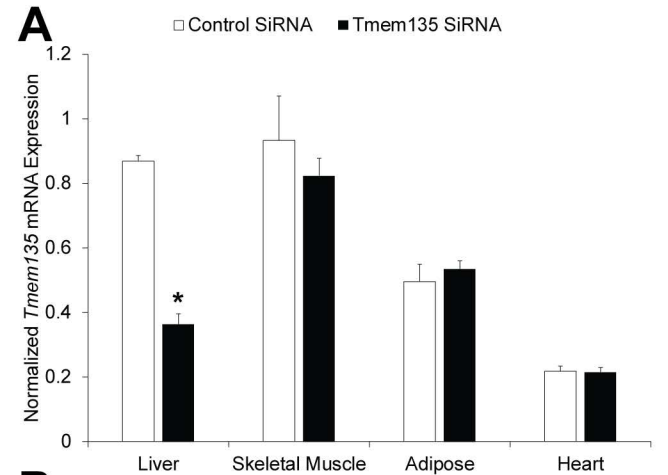
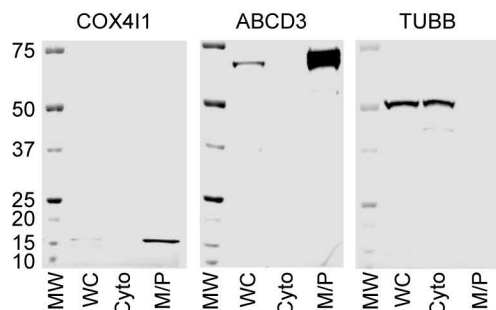
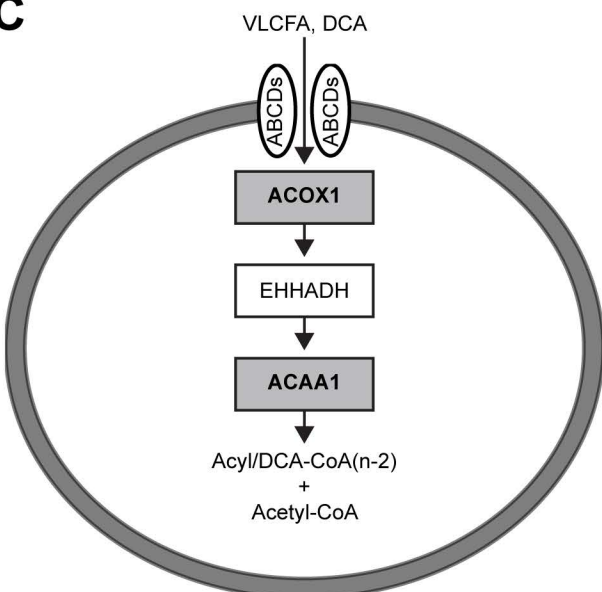
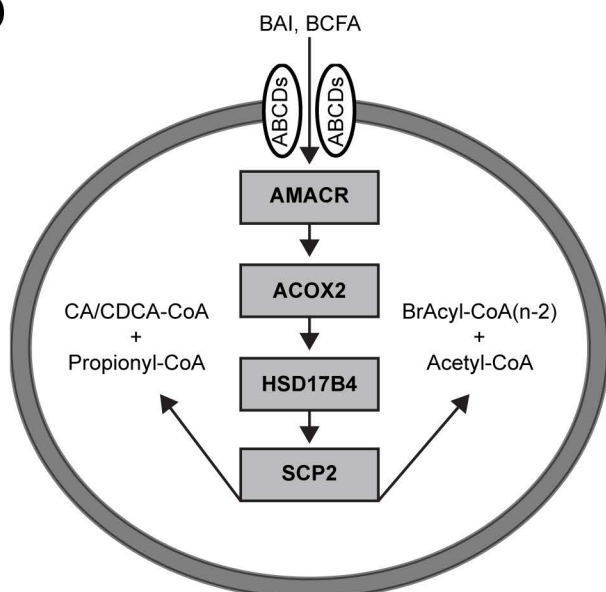
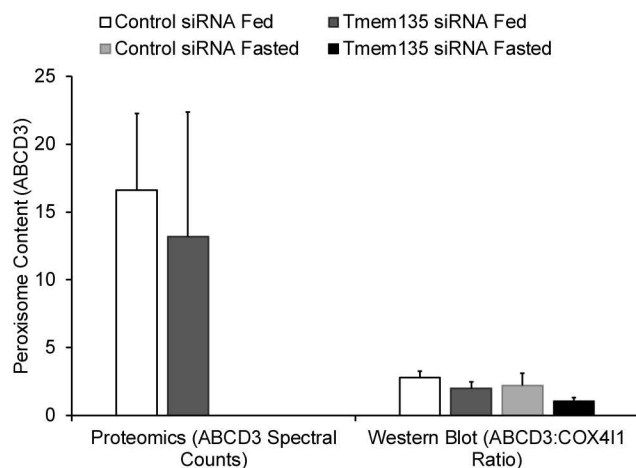
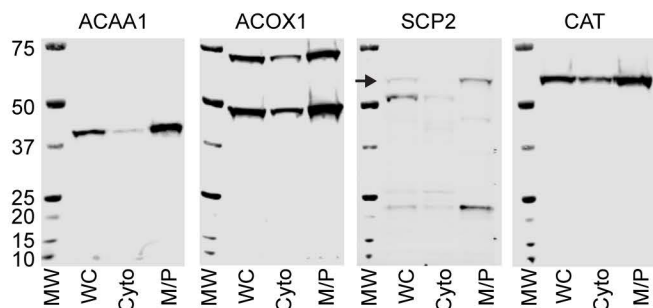
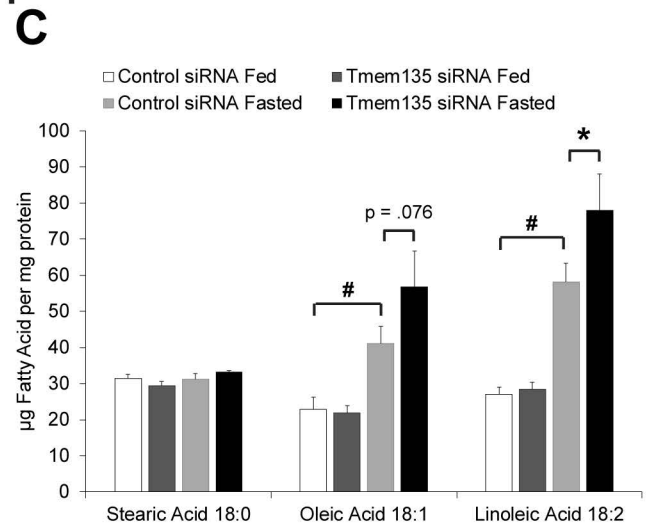
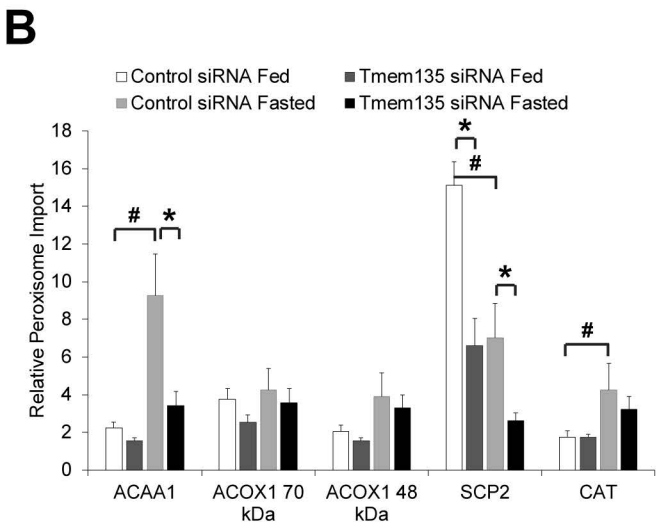
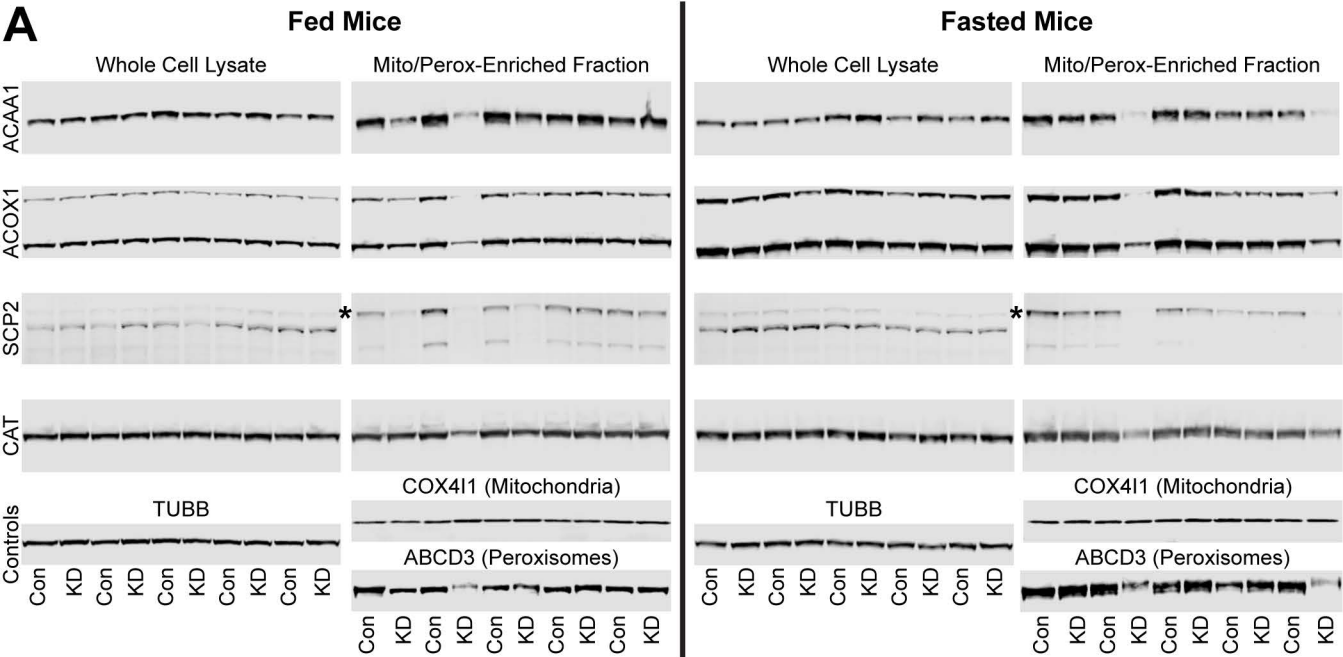


Figure 5

A**B**

Protein Symbol	Weighted Spectral Counts \pm SEM	
	Control siRNA	Tmem135 siRNA
CPS1	110 \pm 16.3	84.7 \pm 34.1
CAT	125 \pm 7.6	76 \pm 14
SCP2	128 \pm 13.1	69.7 \pm 35.3
HSD17B4	66 \pm 8.5	46.7 \pm 9.5
CES1	61.3 \pm 11.8	43.3 \pm 7.2
NUDT7	28 \pm 8.2	17 \pm 17
ACOX1	27 \pm 6.7	13 \pm 10.5
PC	24.3 \pm 3.8	15.7 \pm 4.7
ACOX2	22 \pm 4.4	13.3 \pm 11.9
CES3	17.7 \pm 3.7	10.7 \pm 6.1
GLUD1	21 \pm 2.3	13 \pm 3.1
DHRS4	23.3 \pm 3.4	11.3 \pm 6.4
HACL1	20.7 \pm 3.7	9.7 \pm 5.7
COMT	17.7 \pm 5.8	8.3 \pm 8.3
MTTP	15 \pm 4.7	7.7 \pm 4.3
PSAP	14 \pm 4.5	5.3 \pm 3.2
ACAA1	35 \pm 6.5	9.3 \pm 9.3
ALDH3A2	11 \pm 2.9	5.3 \pm 3.5
ALDH6A1	11 \pm 2.9	5.7 \pm 3.5
AMACR	10 \pm 2.6	4 \pm 4
SUCLA2	9 \pm 1.7	3.3 \pm 2.4
ACADL	5 \pm 0.6	1.7 \pm 0.9
SLCO1A1	3.7 \pm 1.2	1 \pm 1

C**D****E****F****Figure 6**



D

Fatty Acids

	Fed Mice			Fasted Mice		
	Control siRNA	Tmem135 siRNA	P	Control siRNA	Tmem135 siRNA	P
14:0	0.32 ± 0.06	0.29 ± 0.03		0.73 ± 0.12 #	0.85 ± 0.18	
16:0	48.9 ± 3.6	45.7 ± 2.2		70.2 ± 4.4 #	83.1 ± 7.5	^
16:1	2.4 ± 0.5	2.2 ± 0.2		3.5 ± 0.7	5.3 ± 1.0	^
18:0	31.3 ± 1.3	29.4 ± 1.2		31.3 ± 1.6	33.2 ± 0.4	
18:1	22.9 ± 3.4	22.0 ± 1.9		41.1 ± 4.8 #	56.7 ± 9.9	^
18:2	27.1 ± 2.0	28.5 ± 1.9		58.1 ± 5.1 #	78.0 ± 10.0	*
20:3	2.2 ± 0.2	2.1 ± 0.2		1.1 ± 0.1 #	1.6 ± 0.1	^
20:4	21.0 ± 1.6	19.2 ± 1.4		20.8 ± 1.1	23.4 ± 0.7	
22:0	1.7 ± 0.1	1.4 ± 0.1	*	1.4 ± 0.1	1.6 ± 0.1	
22:6	13.0 ± 1.2	11.7 ± 1.0		17.1 ± 1.1 #	19.0 ± 0.9	
24:0	1.01 ± 0.03	0.83 ± 0.05	^	0.95 ± 0.08	1.01 ± 0.05	
24:1	0.87 ± 0.04	0.87 ± 0.05		1.0 ± 0.1	1.19 ± 0.06	^
Total	172.5 ± 12.9	164.1 ± 7.7		247.4 ± 14.2 #	304.8 ± 28.3	*

Figure 7